A determination of the molar gas constant *R* by acoustic thermometry in helium

R. M. Gavioso[1], D. Madonna Ripa[1], P. P. M. Steur[1], C. Gaiser[2], D. Truong[3], C. Guianvarc'h[3], P. Tarizzo[1], F. M. Stuart[4], R. Dematteis[1]

[1] Istituto Nazionale di Ricerca Metrologica, Strada delle Cacce 91, 10135 Torino, Italy

[2] Physikalisch-Technische Bundesanstalt (PTB), Abbestrasse 2-12, 10587 Berlin, and Bundesallee 100, 38116 Braunschweig, Germany

[3] Laboratoire commun de métrologie LNE-Cnam (LCM), 61 Rue du Landy, 93210 La Plaine-Saint-Denis, France

[4] Scottish Universities Environmental Research Centre, Scottish Enterprise Technology Park, Rankine Avenue, East Kilbride, G75 0QF, UK

Abstract

We have determined the acoustic and microwave frequencies of a misaligned spherical resonator maintained near the temperature of the triple point of water and filled with helium with carefully characterized molar mass $M = (4.002\,6032 \pm 0.000\,0015)$ g mol^{-1}, with a relative standard uncertainty $u_r(M) = 0.37\times10^{-6}$. From these data and traceable thermometry we estimate the speed of sound in our sample of helium at $T_{TPW} = 273.16$ K and zero pressure to be $u_0^2 = (945\,710.45 \pm 0.85)$ m^2 s^{-2} and correspondingly deduce the value $R = (8.314\,4743 \pm 0.000\,0088)$ J mol^{-1} K^{-1} for the molar gas constant. We estimate the value $k = R/N_A = (1.380\,6508 \pm 0.000\,0015) \times 10^{-23}$ J K^{-1} for the Boltzmann constant using the currently accepted value of the Avogadro constant N_A. These estimates of R and k, with a relative standard uncertainty of 1.06×10^{-6}, are 1.47 parts in 10^6 above the values recommended by CODATA in 2010.

1. Introduction

1.1 Motivation and context

The main motivation of this work is to contribute to the ongoing research effort made in support of the proposed new definition of the kelvin [1]. This has the accurate determination of the Boltzmann constant, k, by multiple experimental methods as a prerequisite, in view of the role of k as the conversion factor between mechanical and thermal energy required by the current choice of the fundamental units of the SI.

In this context, several experimental determinations of k have been recently accomplished. These have been performed by (i) the measurement of a thermodynamic or electromagnetic intensive property of a macroscopic sample of gas, or (ii) the measurement of the electrical noise in a sense resistor, or (iii) the optical measurement of the absorption spectra of simple molecules. Remarkably, developments in all these methods has achieved a significant reduction of uncertainties: acoustic gas thermometry (AGT) now stands at the relative uncertainty level of 1 ppm or below [2, 3, 4, 5, 6], while dielectric constant gas thermometry (DCGT), refractive index gas thermometry (RIGT), Johnson noise thermometry (JNT) demonstrated overall uncertainties at the level of a few ppm [7, 8, 9], and Doppler broadening thermometry (DBT), shows a potential accuracy at the level of a few ppm or below [10, 11]. This outstanding progress in several different primary thermometry techniques is important in view of their possible future application to the practical realization of the newly defined kelvin [12], allowing metrological laboratories across the world to realize a thermodynamic temperature standard by choosing the method which is best suited to the particular facilities, experience and knowledge available in the host institution. Also, the consistency of the results from primary thermometers using different physical principles would provide valuable assurance that there are no major systematic effects hidden in any of the experimental techniques. In perspective, current and future research in primary thermometry aims to demonstrate that the accuracy of different methods can be extended over wide temperature ranges, by contextually reducing the cost and complexity of the experimental techniques.

Within this framework of activities, an AGT experiment was started at INRiM, aiming at achieving low uncertainty determinations of the differences between thermodynamic temperature and temperature on the 1990 international temperature scale (ITS-90), $T - T_{90}$, over the temperature range between the mercury and the indium fixed points (234 K – 430 K). For this work, the AGT is operated in relative mode [13] using speed of sound measurements in helium near the temperature of the triple point of water T_{TPW} as a reference. The good performance demonstrated by the experiment in the initial evaluation of this reference indicated that an absolute determination of the product kT_{TPW} with useful accuracy could be achieved, after the accomplishment of some additional measurements and tests, including an estimate of the average molar mass M of the helium sample used in the experiment. These activities led to the acoustic determination of R and k as described and discussed in the remainder of this work.

1.2 Synopsis of data analysis and results

We have determined the speed of sound in continuously flowing helium, at pressures between 60 kPa and 690 kPa, through a 3-litre internal volume spherical copper cavity which is temperature controlled near T_{TPW}, by measuring several acoustic and microwave resonances of the cavity at each pressure.

From the analysis of the complete set of microwave results, which comprises nine triply degenerate modes in the frequency range between 1.45 GHz (TM11) and 10.79 GHz (TE16), we estimated the mean internal radius of the cavity at zero pressure, T_{TPW}:

$$a_0 = (90.069\ 276 \pm 0.000\ 024)\ \mathrm{mm}\ , \tag{1}$$

and the volume isothermal compressibility k_T of the cavity at the same temperature:

$$k_T/3 = (7.484 \pm 0.029) \times 10^{-12}\ \text{Pa}^{-1} \tag{2}$$

From additional sets of microwave results obtained at variable temperatures in the range between 235 K and 303 K, we estimated the linear coefficient of thermal expansion α_{th} of the cavity as:

$$\alpha_{\text{th}} = (1.641 \pm 0.006) \times 10^{-5}\ \text{K}^{-1} \quad . \tag{3}$$

Together, these estimates govern the variation with pressure and temperature of the cavity radius

$$a(p,T) = a_0 \left(1 + \alpha_{th}(T - 273.16)\right)\left(1 + \frac{k_T}{3} p\right)^{-1}, \tag{4}$$

which is needed to calculate the speed of sound in helium at different pressures, and 273.16 K, from the acoustic frequency data recorded along the isotherm.

The complete recorded set initially comprises nine acoustic radial modes (0,2) to (0,10) measured between 60 kPa and 690 kPa. Upon correcting the experimental frequencies for all known perturbing effects, the speed of sound data for modes (0,4) to (0,7) between 170 kPa and 690 kPa were selected for the final analysis. Data for modes (0,8), (0,9) and (0,10) were excluded because their frequency and half-width data exhibited clearly deviating trends at low pressures as a result of overlap with neighbouring non-radial modes. The lowest order (0,2) and (0,3) modes were excluded from the final subset because of their evident interference with elastic shell resonances. The choice of a limited pressure range reduces the uncertainty contribution due to the imperfect estimate of the thermal accommodation coefficient *h* in the results of a fit with a linear function of pressure:

$$u^2(p) - A_2 p^2 = u_0^2 + A_1 p, \tag{5}$$

where A_1 and A_2 are respectively related to the 2nd and 3rd acoustic virial coefficients of helium, and the intercept

$$u_0^2 = \frac{\gamma_0 R T_{\text{TPW}}}{M} = (945\ 710.45 \pm 0.85)\ \text{m}^2\text{s}^{-2} \tag{6}$$

represents our estimate of the squared speed of sound in helium at zero pressure and 273.16 K, where γ_0 equals 5/3, and *M* is our estimate of the average molar mass of our helium sample

$$M = (4.002\ 6032 \pm 0.000\ 0015)\ \text{g mol}^{-1}, \tag{7}$$

as estimated from mass spectrometry and the comparative acoustic measurements discussed in section 5. Finally, our estimates of the quantities u_0^2, T_{TPW} and *M* in (6) and the quadrature sum of their corresponding relative uncertainties, as summarized in table 1 provide an estimate for the molar gas constant *R*

$$R = (8.314\ 4743 \pm 0.000\ 088)\ \text{J mol}^{-1}\ \text{K}^{-1}, \tag{8}$$

and, using $R = kN_{\text{A}}$, where N_{A} is the 2010 CODATA value [14] of the Avogadro constant, we deduce the following value for the Boltzmann constant *k* determined in this work:

$$k = (1.380\ 6508 \pm 0.000\ 0015) \times 10^{-23}\ \mathrm{J\ K^{-1}}. \quad (9)$$

Table 1. Summarized budget of the uncertainty contributions to the determinations of R and k

Quantity	Estimate	u_r / ppm
u_0^2	(945 710.45 ± 0.85) m^{-2} s^{-2}	0.90
M	(4.002 6032 ± 0.000 0015) × 10^{-3} kg mol^{-1}	0.37
T	(273.160 05 ± 0.000 12) K	0.42
R	(8.314 4743 ± 0.000 0088) J mol^{-1} K^{-1}	**1.06**
$k = R / N_A$	(1.380 6508 ± 0.000 0015) × 10^{-23} J K^{-1}	**1.06**

The present values of R and k, which are 1.47 parts in 10^6 higher than the corresponding 2010 CODATA values [14], are compared to other determinations obtained by AGT in figure 1. Unless otherwise stated, all uncertainties in this work are standard uncertainties with coverage factor $k = 1$, corresponding to a 68% confidence interval.

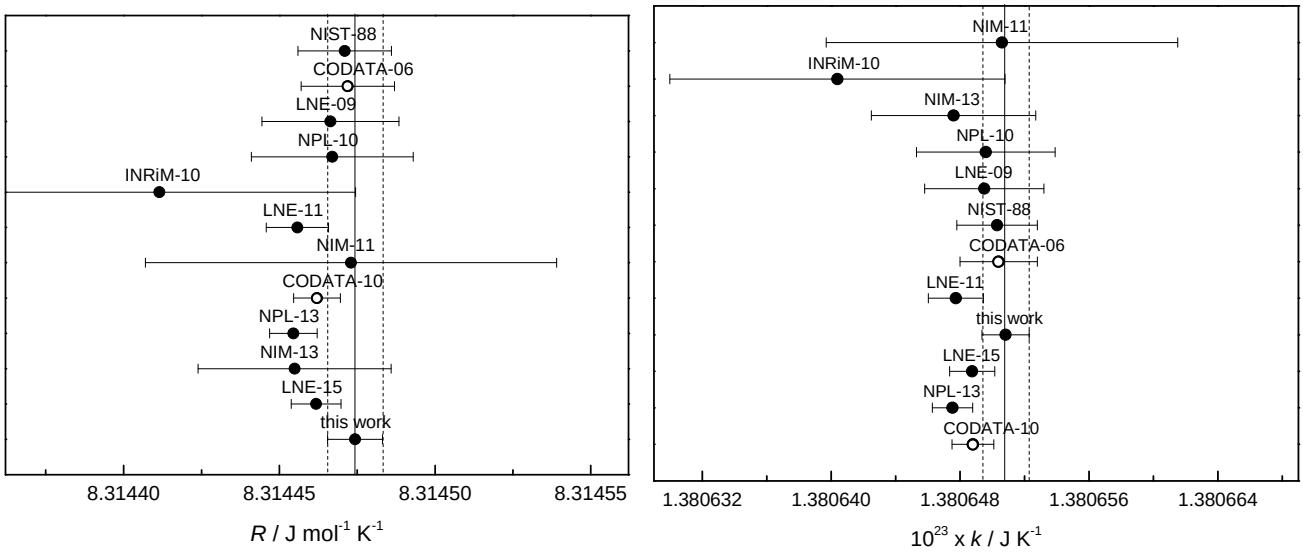

Figure 1. (Left panel) values of the molar gas constant R determined by AGT in chronological order from top to bottom. (Right panel) corresponding values of the Boltzmann constant k in order of decreasing uncertainty from top to bottom. CODATA 2006 and CODATA2010 re-adjusted values are marked with a distinctive symbol. NIST-88 [6]; CODATA-06 [15]; LNE-09 [16]; NPL-10 [17]; INRiM-10 [18]; LNE-11 [4]; NIM-11 [19]; CODATA-10 [14]; NPL-13 [2, 3]; NIM-13 [20]; LNE-15 [5];

1.3 Overview of the technique and organization of the manuscript

The basic principles, techniques and relevant uncertainty contributions of absolute and relative AGT were recently reviewed [15], providing a reference to a more comprehensive discussion of the assumptions, methods, supporting models and results than can be illustrated here.

In the initial part of section 2 we describe the salient design features of the resonator and the results of a characterization, by coordinate measurement machine (CMM), of the dimensions and shape of the two hemispheres that comprise the assembled cavity. In contrast to other experiments which recently achieved accurate determinations of k using ellipsoidal or cylindrical cavities [3, 5, 10], the internal geometry of our assembled resonator was designed to be nearly spherical. Given this

choice, the lifting of the degeneracy of the microwave modes which is needed for their precise measurement is obtained by a micrometric intentional misalignment of the two hemispheres. The remarkable consistency of a microwave determination of the internal radius of the resulting geometrical shape, with data from several modes, represents a positive test of the validity of our design, as described in section 3. Later in section 2, we illustrate the main distinctive features of the instrumentation and the experimental configuration, with emphasis on the description of the system used to measure and control gas pressure and flow rate.

In the remainder of the manuscript we present and critically discuss the mutual consistency and the uncertainty of the results on which our determination of R and k is based. In particular, the measurement procedure and the analysis of microwave data which leads to the results and the uncertainties in (1–3), are illustrated in section 3; the model used to correct the experimentally observed acoustic frequencies and the final fitting procedure leading to (5, 6) and the associated uncertainties are discussed in section 4. The purification procedure used to minimize the contamination of the helium, and the measurements of the contamination levels are described in section 5, including the sampling procedure for mass-spectrometric analysis and its results, and a discussion of the overall uncertainty affecting the estimate in (7). Section 6 discusses the instrumentation and the calibration procedures used to link the average temperature of the gas inside the cavity, using capsule-type standard platinum resistance thermometers (cSPRTs), to the current definition of the kelvin, as realized at INRiM, along with the overall uncertainty of our temperature measurements.

2. Experimental apparatus and measurement techniques

2.1 Design, fabrication and mechanical dimensional characterization of the resonator

The resonator used in this work was constructed from two nominally identical hemispheres, designed to have an internal radius of 90.000 mm. The hemispheres were fabricated at Savimex[1], in electrolytic copper (ETP-Cu), by two procedures of progressively finer machining on a numerically controlled lathe, alternated with stress relieving heat treatments, before final precision turning of their internal shape and their mating equatorial flanges on a temperature controlled lathe equipped with a diamond tipped-tool bit. A diamond turned, cylindrical aluminum holder was bolted to each hemisphere for mounting in the vacuum chuck of the lathe. This procedure was expected to guarantee maximum shape errors of ± 2.0 μm and a surface finish of 10 nm, as declared by the manufacturer. To completely remove scratches left from the initial rougher machining, the final diamond cut increased the internal radius of both hemispheres to (90.100 ± 0.003) mm at 20 °C, as estimated by preliminary CMM measurements.

In order to check that the machined hemispheres were free from relevant shape errors, upon completion of machining, they underwent careful CMM dimensional measurements at the National Physical Laboratory (NPL) using the procedures, instrumentation and expertise previously developed for the dimensional characterization of similar hemispheres [21]. The procedure included comparative measurements with a silicon sphere of well-characterized shape and volume, previously used as a density standard, to estimate scale errors and probe anisotropy of the CMM.

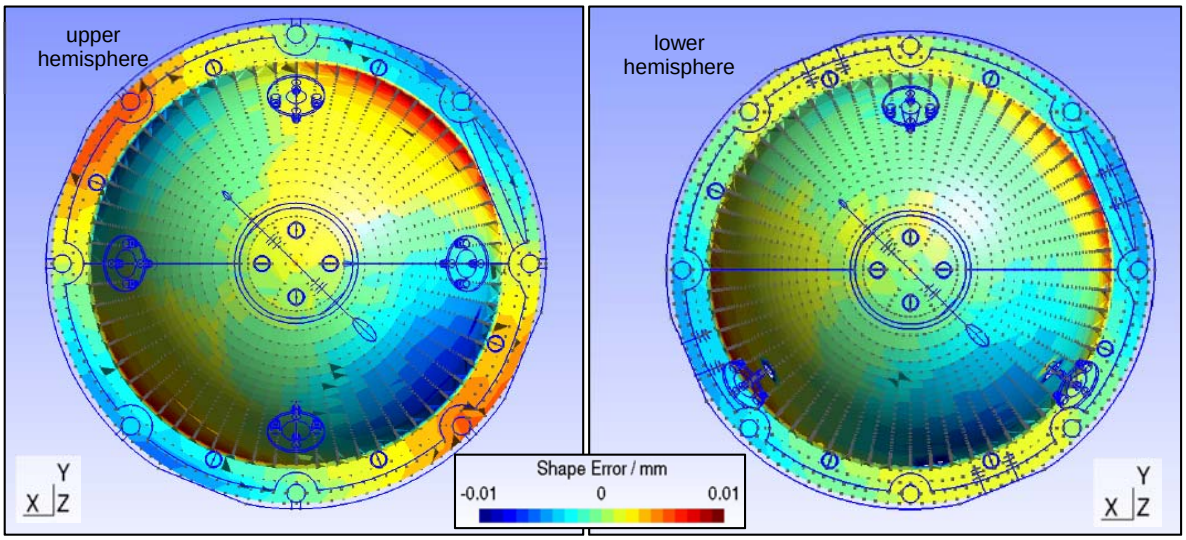

Figure 2. Deviations from sphericity and planarity of the internal surface and the equatorial flange of the two hemispheres comprising the resonator as revealed by the analysis of a large set of CMM data points (dots).

Figure 2 summarizes the most significant information obtained by a dataset of about 2500 measurement points per each hemisphere in the form of a colour map which is scaled to the observed shape errors with respect to mean fitted surfaces. From this representation we observed that, while most of the points on the internal surface showed deviations from sphericity within ± 2 μm, larger deviations from planarity affected the equatorial flanges. These deviations were found to be nearly sinusoidal as a function of the azimuthal angle φ with periodicity 2φ and mean approximate amplitudes of ± 3.5 μm and ± 2.0 μm for the two hemispheres. The cause of this defect was not identified, though we speculate that it might have been caused by elastic deformation of the

[1] Savimex Parc d'activité des bois de Grasse, 06310 Grasse, France

hemispheres by excessive force exerted by the bolts used to fix them to the chuck holder during final machining.

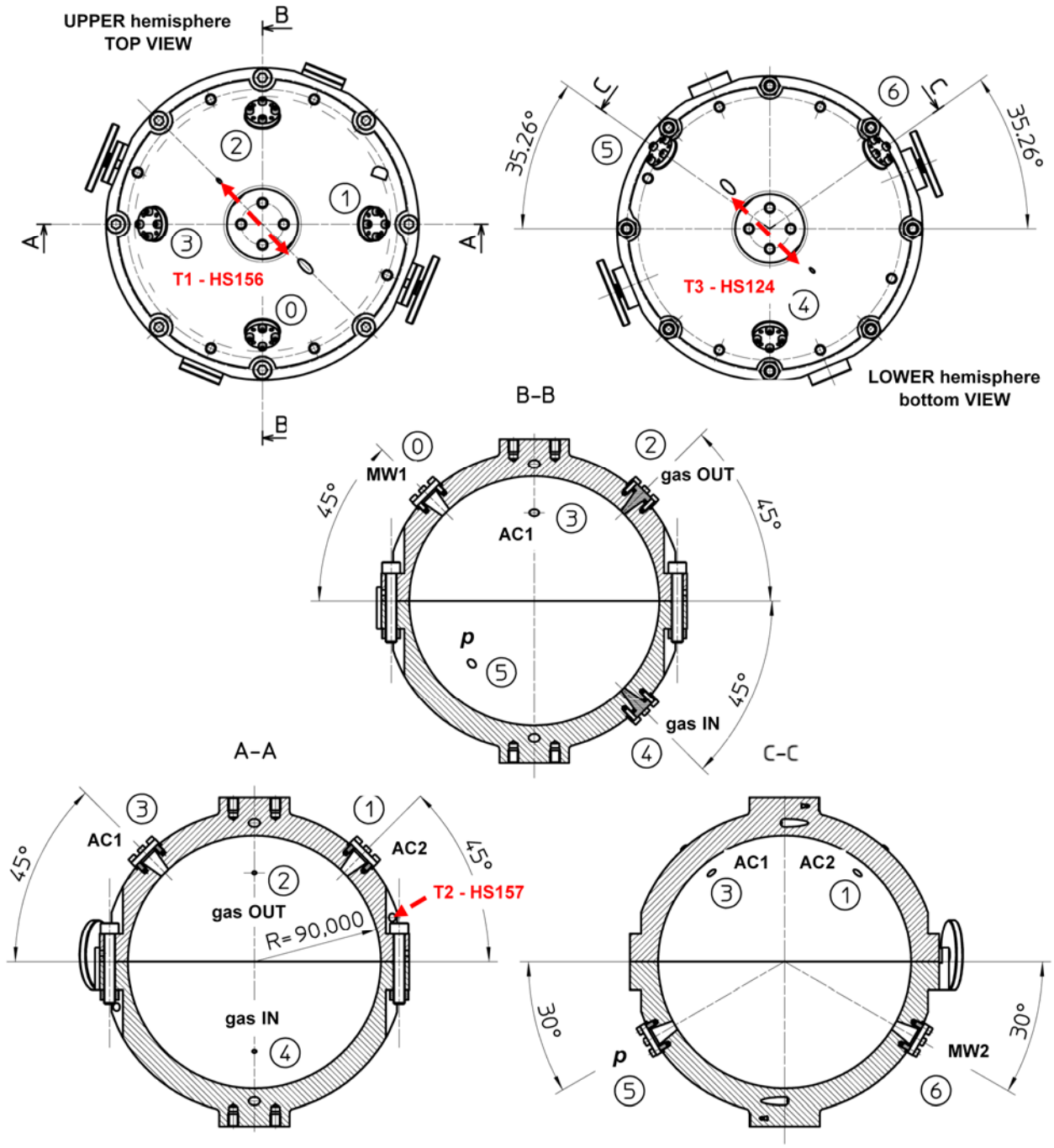

Figure 3. Sketch of the assembled resonator and cross-sections showing the relative position of thermometers (T) acoustic (AC) and microwave (MW) transducers and inlet, outlet and pressure (p) duct connections to a gas manifold.

The complete dataset of CMM measurements for the internal surface of each hemisphere was analyzed by regression with a spherical harmonic expansion [22], providing an estimate of their equivalent radii at 20 °C: a_{eq}^{up} = (90.098 603 ± 0.000 394) mm and a_{eq}^{low} = (90.098 220 ± 0.000 225) mm, where the superscripts *up* and *low* identify the upper and lower hemisphere when assembled in the apparatus. For these results, the reported uncertainties are statistically determined from the

regression, and are not representative of the overall uncertainty which is dominated by much larger type B contributions from the CMM instrumentation and procedure. Though these type of contributions may in principle be significantly reduced [21], their assessment requires an estimate of the elastic deformation of the assembled cavity upon tightening of the equatorial bolts, and the amplitude of the equatorial gap caused by the imperfect flatness of the mating equatorial flanges. A careful evaluation of these effects was not attempted here. However, we remark that the microwave estimate of the cavity radius as a function of temperature, as anticipated in (1) and (3), agrees fortuitously well with our incomplete CMM estimate, being about 500 nm larger than the mean of a_{eq}^{up} and a_{eq}^{low} .

At an intermediate step in the course of the machining procedure, seven conically tapered ports were bored through the wall of the resonator. Five of these ports, with nominally identical shape and dimensions can accept matching adapters to support microwave waveguides and antennas or, alternatively, 1/4-inch condenser microphones. The varied distribution and angular positioning of these ports across the two hemispheres allowed the relative position of two microphones and two antennas to be chosen from a great number of combinations. The final position of the acoustic and microwave transducers (figure 3) was selected, by trial and error, to minimize the overlap of purely radial acoustic modes with neighbouring degenerate modes, and to achieve efficient excitation and detection of all the components of triply degenerate TM and TE microwave modes. The two remaining ports were designed to accept mounts for gas inlet and outlet ducts. Their relative position on the assembled resonator (figure 3) was chosen to ease mixing of the in-flowing gas before leaving the cavity through the outlet duct.

A complete set of matching blank copper plugs were mounted in the corresponding ports, with their front surface initially slightly protruding beyond the cavity surface, during the final diamond turning of the hemispheres. After the final cut, the mounted plugs were not visible by eye, nor was a relevant discontinuity of their front surface position with respect to the surrounding cavity surface detected by probing CMM measurements (figure 2). For measurements, the blank copper plugs were replaced by a set of carefully machined replicas (figures 5, 7, 8) bored along their axis to adapt mounting of two 1/4-inch condenser microphones, two microwave cables terminated to form antennas; two variable section ducts for flowing gas in and out of the cavity by connection to a gas manifold and one duct directly leading from the cavity to a pressure transducer. The design features and the dimensions of these adapters are described in the following sections.

2.2. Preparation of the resonator

The resonator was initially assembled by coarsely aligning the two hemispheres in a position determined by the match of mating equatorial flanges. Using a system composed of four fine-threaded knobs positioned 90° apart on the side vertical edge of the flanges (figure 4), we then finely adjusted the relative position of the two hemispheres, while simultaneously observing the microwave response of the cavity from a few triply degenerate TM and TE modes. In the course of this adjustment, the relative frequency separation of the single peaks within the triplets could be varied significantly (over two orders of magnitude), in proportion to misalignment. Also, the perturbing effect induced by increasing misalignment was observed to be approximately linear and symmetric (equal and opposite in sign) for the higher and lower frequency components of each triplet. The simple mechanical system used to vary the relative position of the hemispheres was not suitable to transform these qualitative observations into an independent mechanical estimate of the variable geometry of the assembled cavity, and no attempt was made to characterize the resulting perturbation on the microwave field quantitatively. Instead, the alignment procedure was simply terminated when the relative separation of the triplets was close to an observable minimum, but still wide enough to obtain stable, precise and robust fitting results for all the investigated triplets (section 2.3). The final relative position of the hemispheres was fixed by tightening the equatorial bolts. The progressively increased torque applied to the bolts was observed to increase the mean frequency and decrease the mean half-width of the triplets. These changes are similar to others previously reported [21] and were interpreted to be a

reduction of the internal dimensions of the cavity, mainly along its vertical axis. Increase in the torque was stopped when no further variation of the microwave parameters was observed. The geometrical interpretation of microwave results, based on data recorded in controlled temperature and pressure conditions, is discussed in section 3.3.

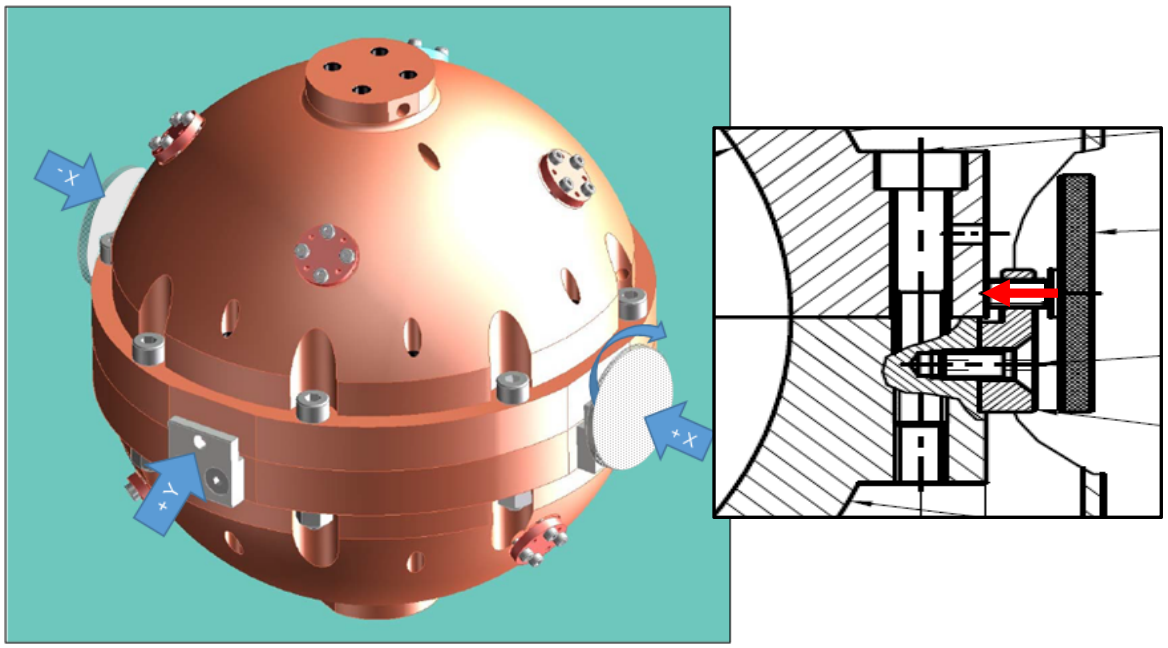

Figure 4. Sketch of the assembled resonator showing the simple mechanical system (cross sectioned in frame) used to adjust the relative position of the two hemispheres.

2.3. Microwave probes and instrumentation

Two different types of antennas (figure 5) were prepared. The first type (figure 5a), a straight probe obtained by cross cutting a section of semi-rigid RG405 coaxial cable (o. d. 2.26 mm), was snugly inserted and fixed in a bored copper microwave adapter so that the central cable conductor, the surrounding PTFE dielectric, and the external copper shield were all flush with the front part of the adapter and the cavity surface. This type of probe weakly couples to TM modes, however, the

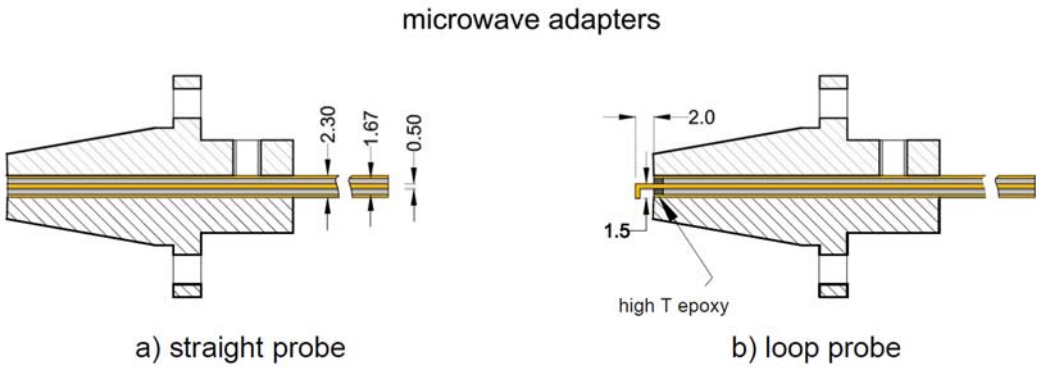

Figure 5. Cross section of microwave adapters and antennas.

perturbations induced by its coupling with the microwave field within the cavity are well known and calculable from previous work [23]. The second type (figure 5b), was prepared from the same cable by stripping back the PTFE dielectric for a length of 1 mm, and filling the tiny resulting volume with

a temperature resistant epoxy resin (Epotek 353ND)[2]. The central conductor was left protruding within the cavity by approximately 2 mm and was bent at a right angle for 1.5 mm. This design allowed efficient detection of both classes of TM and TE modes, but does not allow a reliable calculation of the perturbation induced on the microwave field. In the course of a preliminary substitution test (section 3.1), this perturbation was estimated by comparing the difference in the microwave response of the two probe types.

Standard instrumentation and procedures, based on the use of a network analyzer (Agilent E5071C) locked to a suitable frequency reference (SRS FS725), were used to record microwave data by a scan of 201 frequencies spanning the resonance curves of several triply degenerate modes. These data were fitted to the sum of three resonance functions plus a quadratic background, for a total of 18 adjustable parameters [15]. The variable geometry of our misaligned resonator allowed us to lift the degeneracy of the triplets to a variable extent. In our final configuration the separation of the single peaks varied between $3g_N$ for mode TM11 to $5g_N$ for mode TE16, where g_N is the measured half-width of each singlet. The corresponding frequency separation between the highest and the lowest peak of the TM11 mode was ± 60 kHz with respect to its mean frequency of 1.453 GHz, or relatively ± 40 ppm; the relative separation of the peaks of the TE16 mode at 10.45 GHz was ± 20 ppm. As an example of the precision which is achievable in this condition, figure 6 shows the recorded data and the results and the residuals of a fit to mode TM15.

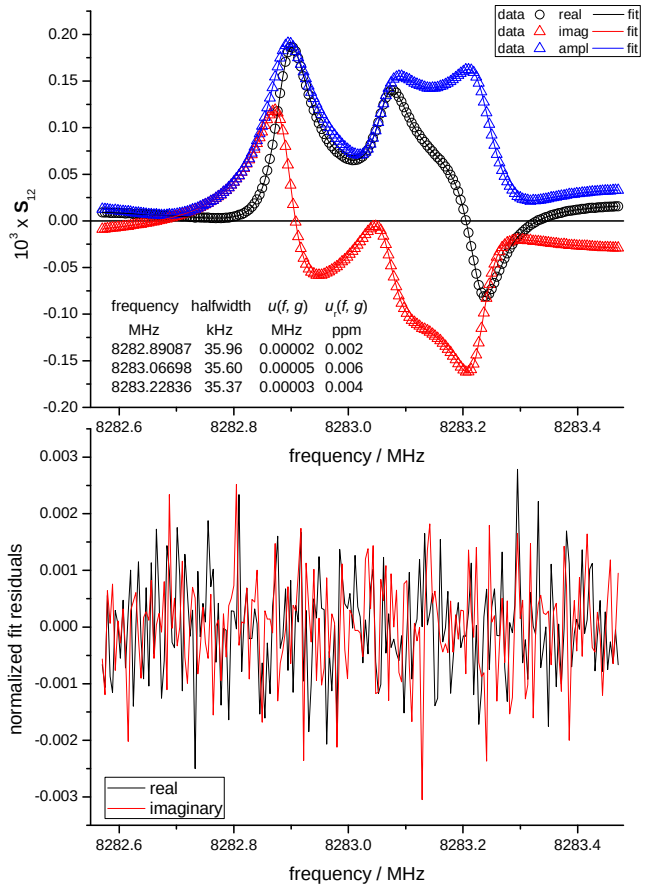

Figure 6. Data and fitting results and residuals for the microwave resonance TM15 at ambient temperature.

[2] Identification of commercial equipment and materials in this paper does not imply recommendation or endorsement by INRiM, PTB, LNE-Cnam or SUERC nor does it imply that the equipment and materials identified are necessarily the best available for the purpose.

To increase our confidence that the fitting results are accurate at the same level of precision we performed tests with synthetic data which were prepared using the same function used for fitting, with the addition of pseudo-gaussian noise to simulate the characteristic features of an experimental resonance in terms of frequency separation and signal to noise ratio. The results of tests where the halfwidths were progressively increased up to a factor five with respect to their original value, confirmed that, even in this strongly overlapping condition, the fitting results were always consistent with the synthetized parameters.

2.4. Acoustic transducers and instrumentation

We used two 1/4-inch condenser microphones (G.R.A.S. 40 BF) to excite and detect the acoustic field within the resonator. These transducers were mounted into copper adapters (figure 7) which were precisely bored along their axis to minimise the presence and the perturbation from annular gaps between the microphone cartridge and the adapter, and are internally threaded to facilitate the precise alignment of the front part of the microphone with the internal surface of the resonator. The resulting alignment is necessarily imperfect as the mechanical connection between the front outer rim of the microphone body and the membrane has a convoluted radial profile of variable height. We used an optical microscope equipped with a position readout system (5 μm resolution) to estimate this profile and calculate the change in volume that was caused by the replacement of each blank plug with its corresponding microphone adapter (section 3.1).

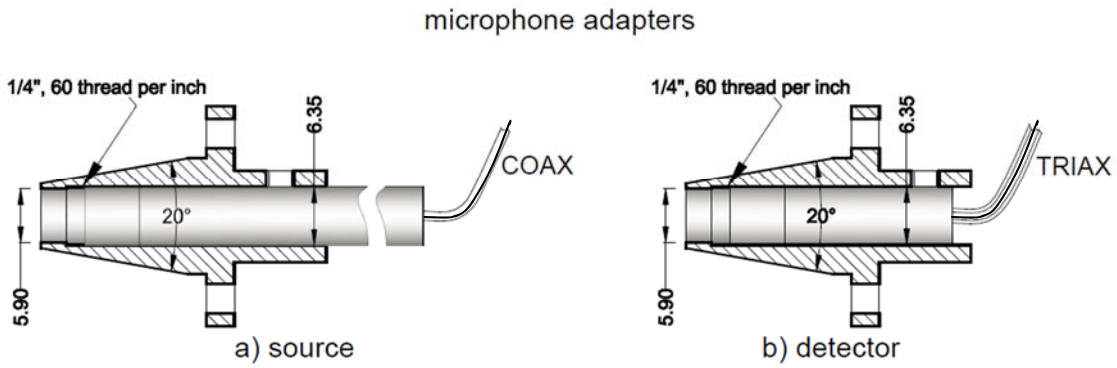

Figure 7. Cross section of acoustic adapters and microphone connections.

The measurement of the first nine (0,2) to (0,10) purely radial modes of the cavity at 273.16 K, occurs in the frequency range 7.74 kHz < f < 51.4 kHz. The electrical sinusoidal signal fed to the source microphone, left unpolarized, was synthesized at 2f, with an amplitude of 1 V_{RMS}, by a waveform generator, locked to the same frequency reference used by the network analyzer, and successively amplified to approximately 95 V_{RMS} using a high gain, high voltage electrostatic actuator amplifier (G.R.A.S. 14 AA). This arrangement minimizes electrical cross-talk between the source and the detector microphone. The latter is triaxially connected to a 1/4-inch preamplifier through a microphonic voltage supply which allows the polarization voltage V_{pol} of the detector to be set at 200 V or 28 V. Despite a significant reduction of the signal to noise ratio (S/N), the 28 V setting was found to be necessary to avoid occasional malfunction of the detector microphone. Similar malfunctioning, with capacitive microphones damaged by arcing were previously reported [6] and eliminated by setting a 150 V polarization [24]. Although we did not find a convincing explanation for microphonic failure (with no evidence of permanent damage by visual inspection of the detector membrane), we noticed that it did not occur at pressures below 100 kPa. Operating at low pressure allows compensation for the reduction of the quality factor of the acoustic modes by conducting measurements with V_{pol} = 200 V.

Standard instrumentation and procedures [15], based on the use of a lock-in analyzer with the reference input set at 2*f*, were used to measure and fit acoustic data.

2.5 Control of pressure and flow

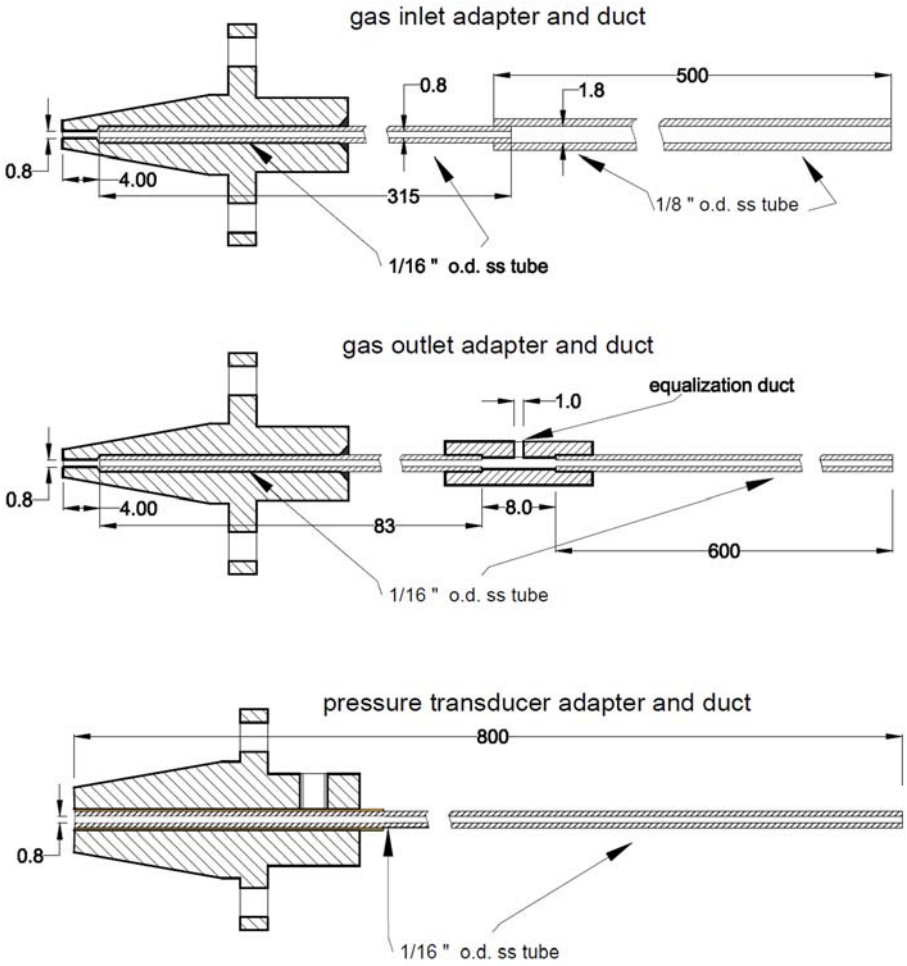

For operation at controlled variable pressure, the resonator is enclosed in a vacuum- and pressure-tight cylindrical steel vessel. The resonator is attached to the top flange of the vessel, in a suspended position, by four stainless steel M6 tension rods clamped on the upper cylindrical boss. This provides a weak thermal link to the surrounding thermostatting bath (Section 6.1).

Figure 8. Adapters and ducts used to flow gas in and out of the resonator and for direct connection from the interior of the cavity to a pressure transducer.

A set of electrical feed-throughs positioned on the top flange of the vessel make a liquid-proof connection to the microwave and acoustic transducers and the thermometers installed on the resonator. A set of mechanical feed-throughs on the flange provide a pressure-tight link for three ducts used to connect the interior of the assembled cavity to a gas manifold located outside the bath, at ambient temperature. The ducts are used for flowing gas into and out of the cavity, and for a direct connection from the interior of the cavity to a pressure transducer. They are assembled from single or multiple stages of electropolished stainless steel tubing with variable internal diameters and lengths as shown in figure 8. We discuss the perturbation induced by these ducts on the microwave and acoustic frequencies in sections 3.4 and 4.2.5, respectively.

To contrast the sensitivity of the speed of sound in helium to even sub-ppm fractions of common impurities, the manifold design (Figure 9) was envisaged to minimize and estimate the effects of contamination. In this work, the manifold was used in three ways: 1) during normal operation, to

continuously flow helium at a constant rate of 7.5×10^{-5} mol s^{-1} (100 sccm) from a gas supply, through a mass flow controller (MFC) and a heated zirconium-aluminum getter, across the cavity, to the manifold, using the inlet and outlet ducts. The manifold design allows continuous flow by-passing the MFC, to estimate the possible contamination by chemically reactive impurities; 2) for the evacuation of the cavity and the containing vessel; 3) for isolating the resonator in a no-flow condition in order to estimate the rate of possible water vapor outgassing [25] or contamination from virtual leaks (section 5.2) over long period recordings of the acoustic frequencies. The internal surface of the gas inlet tubing, which may contribute to contamination by outgassing downstream of the getter section was reduced to a minimum.

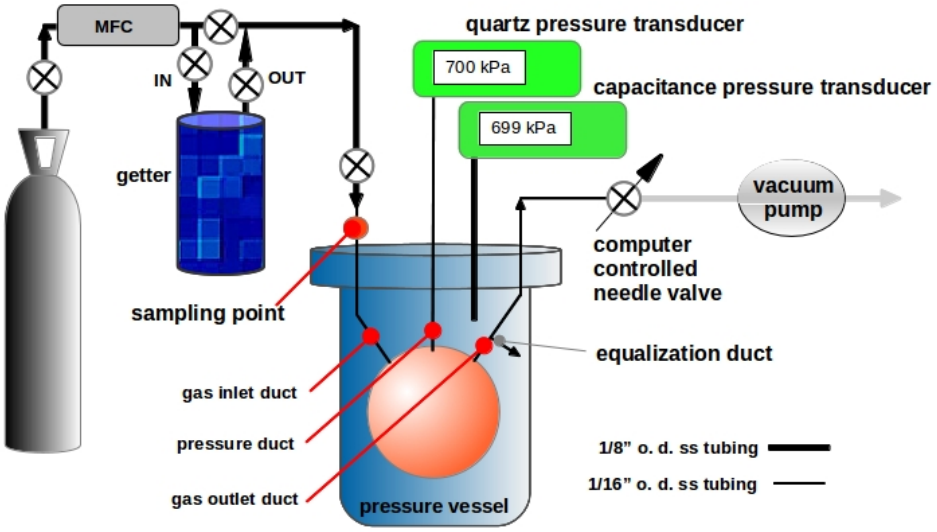

Figure 9. Scheme of the pressure and flow measurement control system.

To eliminate the possible uncertainty arising from an imperfect estimate of the pressure during normal flow conditions, a dedicated duct (0.8 m long, 0.75 mm i.d.) is permanently connected to the resonator and the pressure transducer (Paroscientific Digiquartz 745-100). With this arrangement, the dead volume of this dedicated gas line may now represent a source of pollution directly into the sphere. The experimental tests described in section 5.2 demonstrate that the possible contamination from this source was maintained at an acceptable level.

An auxiliary capacitive pressure transducer was used to monitor the pressure within the vessel. In normal operation, an *equalization* duct bored through the outlet gas tube maintains a small positive pressure difference between the interior of the cavity and the vessel, avoiding drifts or transient relevant pressure gradients across these two volumes.

To control the pressure within the resonator, the outlet section of the manifold comprises an electrically driven needle valve of finely variable conductance. This valve is inserted in a software PID-controlled feedback loop which directly regulates the pressure in the resonator at the level of ± 1 Pa over the whole pressure range of interest for this work.

The evacuating system is composed of a primary membrane pump used to vent the outlet flow preventing back streaming and a turbo-molecular pump for evacuation of the cavity and the vessel.

2.6 Pressure measurements and calibration

The pressure transducer used in this work (Paroscientific 745-100A) is a quartz sensor with a full scale range of 690 kPa, a resolution of ± 0.5 Pa, and an expected accuracy of 0.008 % of the full scale

range, or equivalently 55 Pa, as declared by the manufacturer. The transducer is located approximately 0.7 m above the position of the resonator, with a corresponding head correction of 0.6 Pa at 50 kPa and 8.0 Pa at 690 kPa, which is equivalent to a relative correction of the experimental pressure by 11.6 ppm.

An incorrect estimate of the pressure, or an underestimate of its uncertainty, may affect our determination of R and k in a convoluted way [15], with variable impact depending on the amplitude and trend of the type of pressure error. To get insight on possible errors, the pressure transducer was calibrated against a standard piston gauge used in absolute mode, over the pressure range between 60 kPa and 690 kPa shortly after completing the measurements presented in this work. The mean results of this comparison, based on three repeated cycles, each conducted by taking readings at the calibration points by first increasing and successively by decreasing pressure, are displayed in figure 10. These errors were interpolated with a cubic function of the pressure which was used to calculate pressure corrections to the experimental records before proceeding with data analysis. The overall uncertainty of this correction, which includes contributions from the inherent uncertainty of the reference standard, repeatability and hysteresis, varies between 5 Pa and 10 Pa. We estimated the impact of such a pressure error to our final determination of the squared speed of sound in helium u_0^2 by applying a constant offset of 10 Pa to our experimental pressure records before repeating the calculation of boundary layer corrections and the final fit procedure to our acoustic data (section 4.3). This repetition resulted in a change of our estimated value of u_0^2 by – 0.1 ppm (table 3).

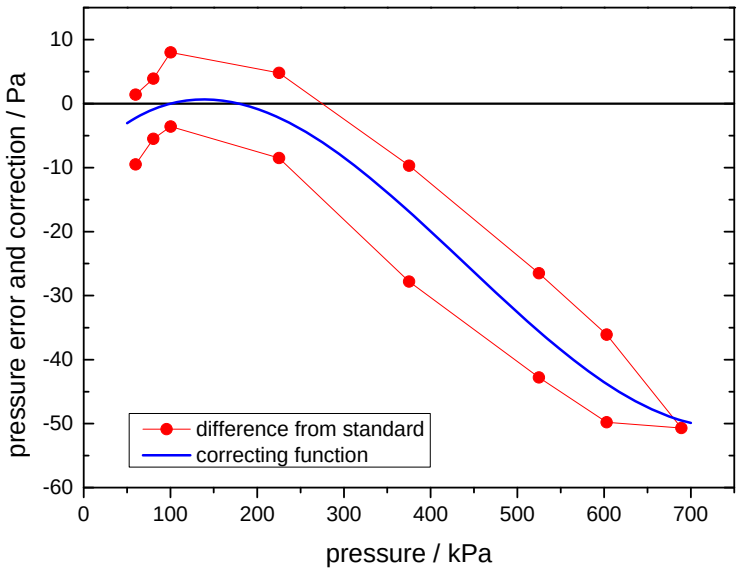

Figure 10. Results of a calibration of the pressure transducer against a standard pressure balance. The red full circles display the absolute pressure differences between the transducer and the standard. The solid line is a cubic interpolating function used to correct the experimentally recorded pressure readings.

2.7 Measurement procedure and datasets

Our determination of R is mainly based on the results of nearly simultaneous measurements of acoustic and microwave frequencies, temperature and pressure, conducted while continuously flowing helium at variable pressures through the resonator, which is held within a few mK of our estimate of T_{TPW}. Altogether these results comprise a single dataset, or *isotherm*, recorded over 15 days, starting at the maximum pressure of 690 kPa (chosen to match the full scale range of the pressure transducer) and continued by progressively reducing the pressure at 18 different steps down to 60 kPa. Following each pressure reduction, a suitable period of time (10 hours) was allowed for the resulting thermal transient to decay before proceeding with the measurements. An additional

recording of the microwave frequencies and temperature, taken while the resonator is being evacuated to residual pressures below 0.01 Pa, completes the data set, providing a direct experimental estimate of the resonator radius whose consistency can be checked with the result of an extrapolation of microwave data to zero pressure. The low conductance of the manifold connecting the pumps to the resonator was found to require at least 24 hours of continuous evacuation before a stable estimate of this quantity could be achieved.

At each pressure step, we repeatedly recorded temperatures, pressures and frequencies of several acoustic and microwave modes over an interval of 9.5 hours, which is the time needed for 24 consecutive acquisitions and fitting of a complete set of nine acoustic modes. The analysis of all these redundant data allowed verification of the expected correlation between small variations of frequencies and temperature and to compute mean experimental values and the associated standard uncertainty of each acoustic and microwave mode at each pressure (online supplement), after correcting to 273.16 K, using

$$f\left(p_i, 273.16\right) = f\left(p_i, T_i\right)\frac{u\left(p_i, 273.16\right)}{u\left(p_i, T_i\right)}, \tag{10}$$

for the acoustic frequencies, and

$$\left\langle f\left(p_i, 273.16\right)\right\rangle = \left\langle f\left(p_i, T_i\right)\right\rangle\left[1-\alpha_{\text{th}}(273.16-T_i)\right] \tag{11}$$

for the average frequencies of microwave triplets. In these corrections, which introduce negligible additional uncertainty, $u(p, T)$ is calculated from the independently known thermodynamic properties of helium, and α_{th} is a preliminary estimate of the linear thermal expansion coefficient of the cavity.

Finally, before proceeding with the final extrapolations to zero pressure, the microwave and acoustic frequency datasets prepared by this procedure need to be corrected for all known perturbing effects (online supplement), as discussed in section 3 and section 4, respectively.

3. Microwave determination of the mean resonator radius

Throughout this work we refer to an ideal quantity, denominated mean radius *a*, which characterizes the internal dimensions of our resonator, and is defined as the radius of a perfect sphere of internal volume $V = 4\pi a^3/3$, supposed to be equivalent to the internal volume of our imperfectly spherical cavity as determined by the experimental conditions. For the sake of an acoustic determination of *R*, we make an additional assumption, i.e. that the same volume *V* delimits mechanically the acoustic field and electrically the microwave field. To fulfil the latter assumption, we need to correct the eigenfrequencies of both fields from their perturbed, experimentally measured, f' values to their corresponding unperturbed values f^0. For microwaves, this correction takes the form:

$$\left\langle f^0 \right\rangle = \left\langle f' \right\rangle + \sum \Delta \left\langle f \right\rangle \ . \tag{12}$$

In the following sections we discuss the perturbations considered for inclusion in the sum in (12) and their uncertainty contributions to our microwave determination of the mean radius a_0 at zero pressure, 273.16 K, anticipated in (1). Finally, a_0 is obtained from a linear fit (section 3.5) to the radii calculated from the unperturbed frequencies f^0, upon correcting for the calculated refractive index of helium $n_{\mathrm{He}}(p,T)$:

$$a\left(p,\ 273.16\right) = \frac{c}{2\pi\sqrt{n_{\mathrm{He}}\left(p,\ 273.16\right)}} \frac{z_{\mathrm{m}}}{\left\langle f^0\left(p,\ 273.16\right)\right\rangle_{\mathrm{m}}} . \tag{13}$$

In (13), *c* is the speed of light in vacuum and z_{m} is the eigenvalue of the chosen triplet.

3.1 Microwave perturbations induced by antennas and microphones

The tests described in this section, made to assess the perturbation induced by antennas and microphones onto the microwave field, were conducted while the cavity was at ambient temperature and pressure. To make the results statistically comparable, we kept helium flowing through the resonator at a constant rate, and applied corrections to exactly 100.00 kPa and 296.00 K to account for minor temperature and density variations.

For a first reference test of our microwave measurements, we prepared antennas by simply cross-cutting coaxial cables, and fixed the position of the cut section to be flush with the internal cavity surface (figure 5a). These waveguides coupled very weakly only to the TM modes, causing a minimum calculable [23] perturbation. In figure 11 we plot the radii $a_{\mathrm{TM1}n}$ determined from the frequencies of the modes TM11 to TM15 in this configuration, after applying corrections for all known perturbations. All these determinations are consistent, with a maximum, barely significant difference of 12 nm between the radii determined from modes TM13 and TM15. We notice that the consistency of the mode TM11 with the other TM1*n* sets an upper limit, which we estimate at 15 nm to the thickness of a possible cupric oxide layer on the surface of the cavity [21]; this possibility may lead to an overestimate of the mechanical radius, with a dedicated uncertainty contribution (table 2). Finally, from the measured average half-widths of the triplets $\langle g_{\mathrm{m}} \rangle$ we estimated the resistivity of our copper surface ρ_{Cu} at 296 K to be $(1.772 \pm 0.009) \times 10^{-8}\ \Omega$ m. The corresponding relative excess half-widths for the five modes TM11 to TM15, are displayed in the lower part of Figure 11.

In a second test we replaced the reference waveguides with right angle probes formed by bending a slightly protruding section of the central conductor of the cables (figure 5b). These *loop* probes coupled efficiently to both families of TM and TE modes, with the exception of mode TE11 whose coupling was always too weak to be useful. Also, when the angular position of these probes was definitively fixed for measurements at controlled temperature and pressure, the extremely low

coupling of one of the single components of the TM16 and TE12 triplets, restricted the achievable precision from the recorded data of these modes.

From the comparison of the radii previously determined with waveguides, we observed (figure 11) a mean difference of (21 ± 12) nm for modes TM12 to TM14 and (48 ± 14) nm for the single TM11 mode. These observed differences may be interpreted as a perturbation induced from this specific type of antennas, or as an estimate of the reproducibility of the insertion of any type of antennas in tests conducted at ambient temperature. In table 2 we account for this interpretative limit with a specific uncertainty contribution. The larger difference observed for mode TM11, which was found to be statistically significant in the course of repeated tests, makes this mode inconsistent with all the others, supporting its rejection from our final estimates of the mean cavity radius.

We did not observe any additional energy loss upon the substitution of straight probes with loop probes, with a nearly coincident estimate $\rho_{Cu} = (1.768 \pm 0.005) \times 10^{-8}$ Ω m of the surface resistivity as measured by the half-widths (figure 12) of 10 TM and TE modes.

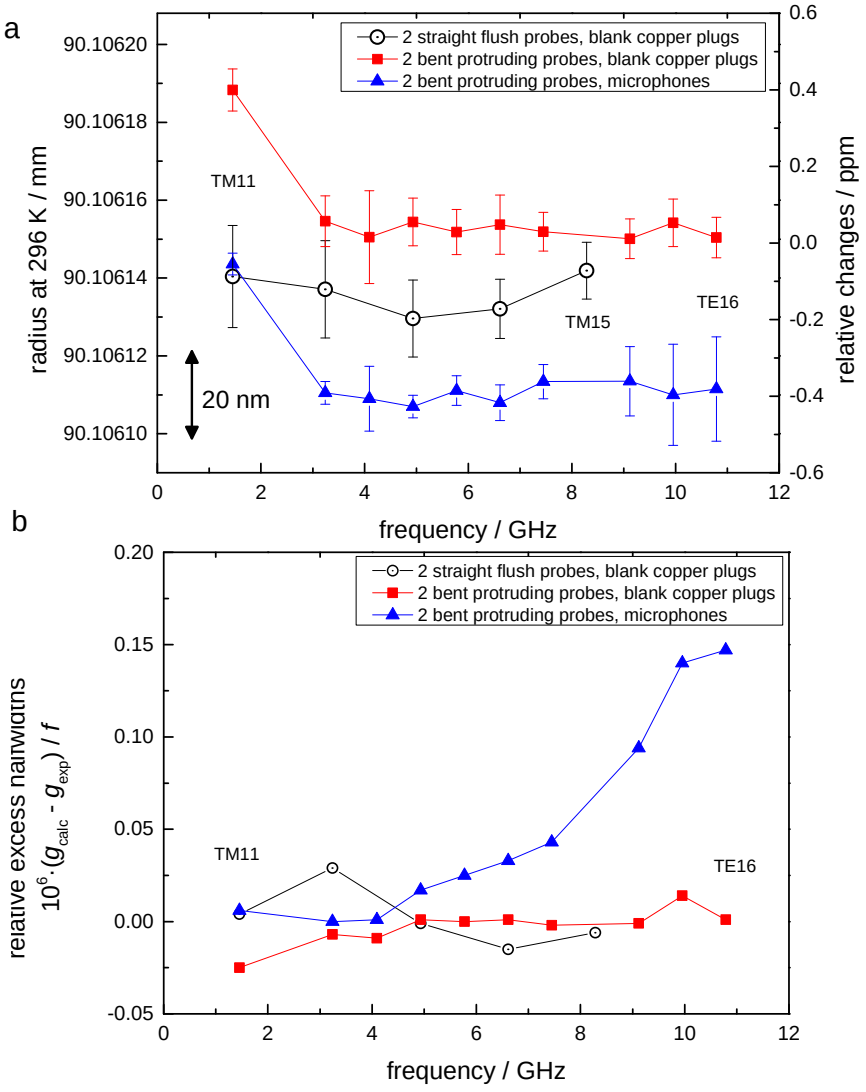

Figure 11. (a) Changes in microwave radii at 296 K, 100 kPa, for three different experimental configurations with two types of antennas and blank plugs or microphones. For every mode in each set the uncertainties are the standard deviation of repeated measurements; (b) Corresponding excess halfwidths, with different copper resistivities estimated from the mode halfwidths in each configuration.

Finally, we discuss the effect of replacing two blank copper plugs with the acoustic transducers, mounted within their adapters (figure 7), in previously characterized (by microscopy) positions. This

replacement was observed to have a twofold effect on the microwave resonances: i) the mean radius varies by (−42 ± 15) nm, in reasonable agreement with the variation of −28 nm expected from our optical estimate of the profile of the microphones within their adapters. The variation of mode TM11 (−44 ± 6) nm is consistent with that of the other modes, as an additional indicator that the surface of the microphones is not significantly protruding or recessing from that of the cavity [4]; ii) the measured resistivity at 296 K increases on average by 4.3 %, and it is no longer consistent for all the modes, increasing smoothly from $(1.845 \pm 0.003) \times 10^{-8}$ Ω m, if determined from the lowest frequency TM11 mode, to $(1.996 \pm 0.006) \times 10^{-8}$ Ω m if determined from mode TE16. This variation is only partially accounted for by the relative variation of 2.5 %, which is expected due to the increase of the mean resistivity of the cavity surface caused by the substitution of copper plugs with microphones made of steel, $\rho_{steel} = 7.5 \times 10^{-7}$ Ω m.

3.2 Skin effect and thermal expansion

We used microwave data from additional isotherms measured in helium between 235 K and 302 K to calculate the variation of the surface resistivity as a function of temperature, in our experimental configuration, i.e. with microphones inserted. When fitted as a linear function of temperature (figure 12) these data provide an estimate of the apparent resistivity in this configuration: $\rho(T) = \rho_0 + \rho_1 (T - 273.16)$ with $\rho_0 = 1.689 \times 10^{-8}$ Ω m and $\rho_1 = 7.0 \times 10^{-11}$ Ω m K^{-1}. To calculate the perturbation due to the finite conductivity of the surface at 273.16 K, we correct this result by first subtracting the increase in surface resistivity due to the insertion of the microphones (previously measured at 296 K) with the intermediate result $\rho = 1.613 \times 10^{-8}$ Ω m, in good agreement with other determinations for the same type of copper [3, 4]. Finally, we correct our estimate of the expected resistivity at 273.16 K, in our experimental configuration, to $\rho = 1.653 \times 10^{-8}$ Ω m to account for the 2.5 % calculated increase of ρ due to steel microphone surfaces.

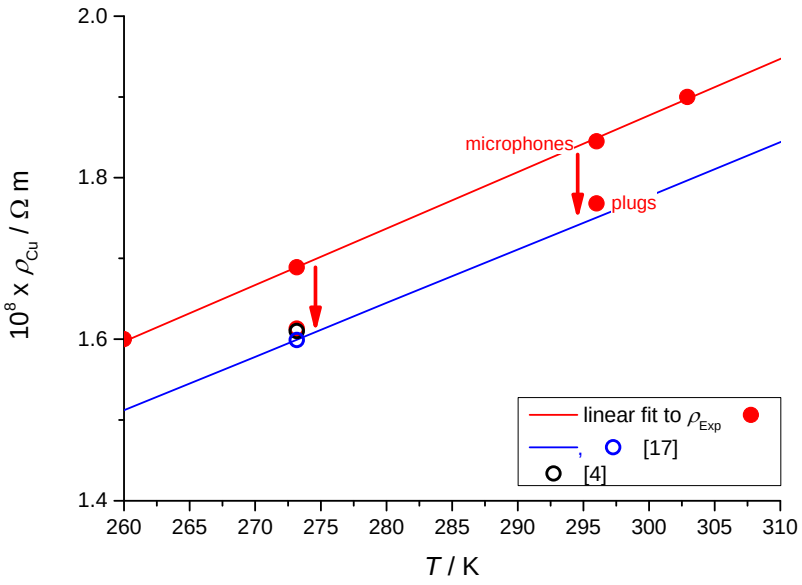

Figure 12. Estimated surface resistivity ρ_{Cu} of the cavity as a function of temperature and comparison, at 273.16 K and 296 K, with previous estimates for the same type of copper [4, 21]. Arrows connecting points at the same temperature show the increase in resistivity due to the insertion of the microphones.

We use this value to calculate the expected mode half-widths g_{calc} at 273.16 K, and evaluate the uncertainty of the skin correction $\Delta\langle f_m \rangle = \langle g_{calc} \rangle$ from the comparison with experimental half-widths measured in vacuum at the same temperature (figure 13). This comparison shows that the relative excess half-width $\langle g_{Exp} - g_{calc} \rangle / \langle f \rangle$ is always less than 0.2 ppm for all modes, with a mean associated

uncertainty of 0.10 ppm (table 2). If this comparison is separately made for the single components of the triplets, none appear to be significantly larger, seemingly indicating a minor influence of the mechanical imperfections at the equatorial joint.

The complete set of microwave data measured as a function of T can be used to define the thermal expansion of the cavity by the estimate of $\alpha_{th} = (1/a)(da/dT) = (1.641 \pm 0.006) \times 10^{-5}$ K^{-1}. This quantity is used to correct microwave data measured at temperatures slightly different from 273.16 K with negligible additional uncertainty.

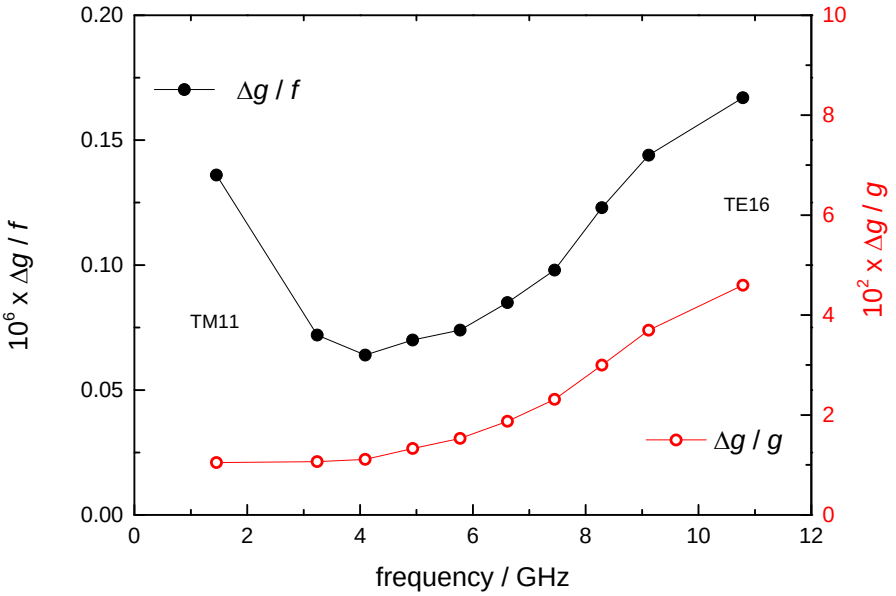

Figure 13. Relative excess half-widths of microwave modes measured in vacuum at 273.16 K. The expected value of the half-widths is calculated using our reference estimate for the surface resistivity $\rho_{Cu} = 1.653 \times 10^{-8}$ Ω m, as corrected for the presence of the microphones. Excess halfwidths are plotted twice with different scales: (left Y-axis– full circles) scaled by frequency in ppm; (right Y-axis– hollow circles) scaled by halfwidth in per cent, to evidence the smooth increase in apparent resistivity for modes at high frequency.

3.3 Geometrical correction

We know that the internal geometrical shape of our assembled cavity is not perfectly spherical because of the intrinsic shape errors of each comprising *hemisphere* which were recorded by the CMM measurements (section 2.1) and, more importantly, because the hemispheres were intentionally misaligned (section 2.2) to lift the degeneracy of microwave modes and enhance the precision achievable in the measurement of their frequency. In these experimental conditions, an estimate of the perturbation induced by the geometrical imperfections onto the microwave eigenfrequencies is needed. An analytical model of the microwave perturbation in quasi-spherical geometries was recently achieved for spheroids and ellipsoids [26, 27], and further generalized for cavities with arbitrary shapes which result from a smooth and sufficiently small perturbation of a spherical geometry [28]. Unfortunately, no model is currently available to account for the non-smooth singularity resulting from the sharp edge formed at the equatorial joint by misaligning two hemispheres. Thus, we make the simplifying hypothesis that the internal shape of our misaligned resonator may be conveniently approximated as an ellipsoid, and test this hypothesis against the effectiveness of its practical application to our experimental data. In assuming the validity of this approximation, we are supported by the observation that the shape parameters ε_1, ε_2 calculated from the observed splitting of the microwave triplets are extremely small and very precisely consistent for all the modes examined: $\varepsilon_1 = (1.969 \pm 0.005) \times 10^{-4}$; $\varepsilon_2 = (1.018 \pm 0.002) \times 10^{-4}$. In fact, the reaction of the microwave modes to misalignment is not discernible from what would be observed in an ellipsoid with semiaxes differing by only 18 μm and 9 μm from the nominal reference of 90 mm.

Additionally, the shape parameters ε_1 and ε_2 were found to be stable over the whole investigated temperature and pressure range.

These small deviations from sphericity determine correspondingly small geometrical corrections to the mode eigenvalues, tabulated in an online supplement to this paper (stacks.iop.org/Met/xxx), which vary between 0.005 ppm for mode TM11 to 0.35 ppm for mode TE16. Altogether these corrections increased our microwave estimate of the mean radius by 13.5 nm, equivalent to 0.15 ppm. In order to estimate the uncertainty associated with the geometrical correction to our estimate of the squared speed of sound in helium, in section 4.2.4 we discuss the combined effect of its application to both the microwave and the acoustic eigenvalues.

3.4 Microwave perturbations by ducts and waveguides

We corrected our measured average microwave frequencies to account for the perturbing effect of two antennas (figure 5b) and three ducts (figure 8) using the models and the results in [23]. However, the effect of the antennas was calculated as if they were simple coaxial waveguides (figure 5a) instead of protruded loops. We note that the possible underestimate of the perturbation which comes from this simplification was accounted for with a dedicated uncertainty contribution, estimated from the change of the mean radius upon substitution of the antennas (section 3.1). The total relative amount of all the corrections for antennas and ducts is less than 0.16 ppm; the uncertainty of this correction is therefore negligible, due to the favourably large ratio between the surface of the cavity and the total surface of the waveguides and holes.

Figure 14 shows the effect of successively applying skin, geometrical, and waveguides and ducts corrections, as tabulated in an online supplement (stacks.iop.org/Met/), to the radii determined from different microwave modes while the cavity was kept under vacuum near 273.16 K. The displayed uncertainties are scaled by the excess half-width of each mode (figure 13) and are not representative of the final uncertainty in our estimate of the radius (section 3.6). Upon rejection of mode TM11, a weighted mean of the data in figure 14, estimates a_0^{vac} = (90.069 277 ± 0.000 003) mm at 273.16 K. This result is in remarkable agreement with an alternative estimate of the same quantity obtained from the extrapolation to zero pressure of microwave data recorded in helium along an isotherm (section 3.5).

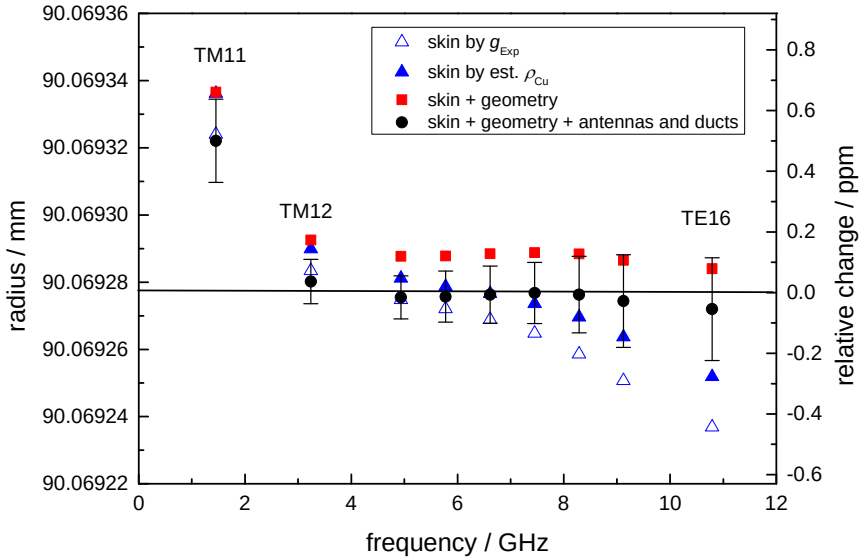

Figure 14. Display of the cumulative effect of several corrections (surface resistivity, geometry, waveguides and ducts) on the estimate of the radii measured in vacuum at 273.16 K. The black line is the weighted mean of 8 modes (TM12 to TE16) with weights scaled by the excess halfwidths of each mode.

3.5 Extrapolation to zero pressure and isothermal compressibility

For helium, several thermophysical properties (online supplement) are calculable from theory with remarkably small uncertainties, making it a useful calibration standard for gas metrology [29]. These properties include the leading terms in a virial equation of state [30, 31, 32], i.e. an accurate estimate of the density ρ as a function of the experimental temperature and pressure. Additionally, calculated values of the polarizability of helium at zero density A_ε [33] and the leading dielectric virial coefficients are also available from theory or experiment [34, 35, 36, 37]. We take advantage of these unique features of helium, and prepare our microwave data, as displayed in the upper part of Figure 15, by applying the corrections for all known perturbations discussed in the preceding section and, using (13), by compensating for the calculated refractive index of helium with negligible additional uncertainty.

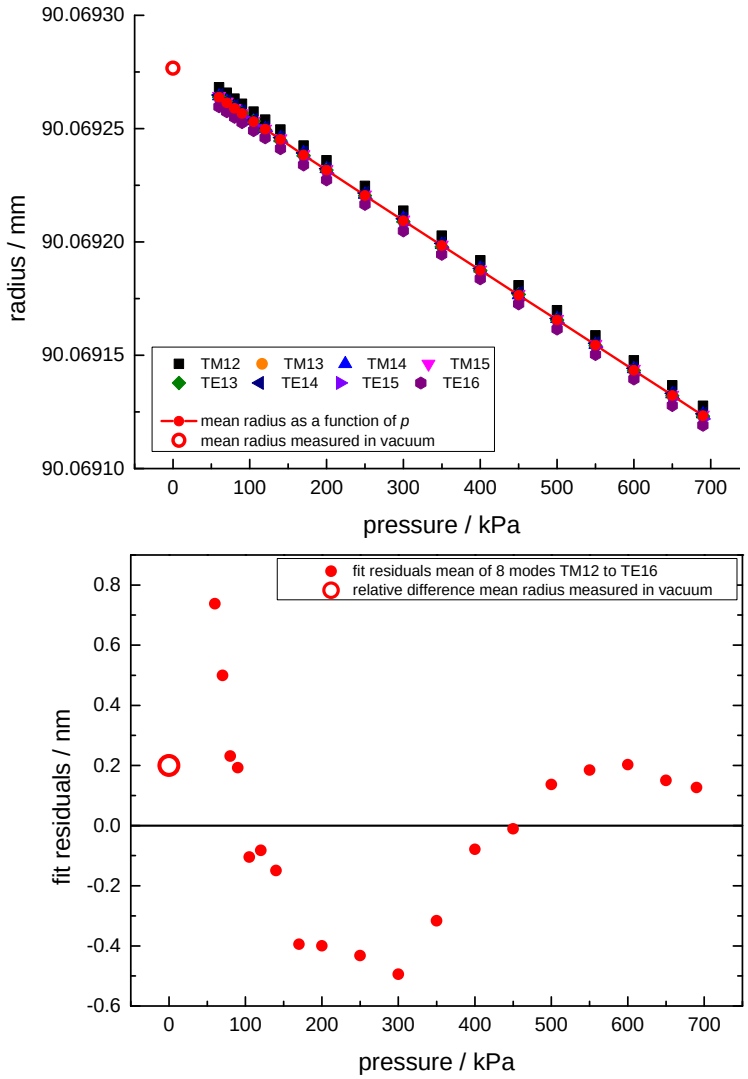

Figure 15. (Top panel) Cavity radius as a function of pressure at 273.16 K. (Bottom panel) residuals from a linear fit (15). The hollow red circle is a direct measurement of the radius of the evacuated cavity; filled red symbols and red line refer to data and residuals from the arithmetic mean of all modes.

These data show the contraction of the cavity internal radius caused by the equal increase of internal (within the shell) and external (in the vessel) pressure. In spite of this being a small effect, the small residuals (± 5 nm for dispersed mode data; < 1 nm for the mean of all modes) displayed in the bottom part of figure 15 highlight the remarkable precision of microwave measurements. The fitted coefficients in:

$$a\left(p,273.16\right)=a_0\left(1-\frac{k_T}{3}p\right)\ , \tag{14}$$

determine: i) our fitted estimate a_0 = (90.069 2765 ± 0.000 0003) mm of the mean radius of the cavity at zero pressure, 273.16 K, with negligible uncertainty from the fit, and consistent with our estimate of the same quantity by a direct measurement in vacuum, a_0^{vac} ; ii) the elastic compliance of the shell $k_T = (3/a)(\mathrm{d}a/\mathrm{d}p)$ with the result $k_T/3 = -(7.484 \pm 0.029) \times 10^{-12}$ Pa^{-1}, previously reported in (2), and consistent with an other determination of the same quantity for a copper cavity [38].

3.6 Uncertainty budget and final microwave estimate of the cavity radius

Table 2 summarizes the relevant (larger than 0.05 ppm) uncertainty contributions to our microwave determination of the resonator radius.

Table 2. Uncertainty budget for microwave determination of the squared cavity radius

Source	$u(a_0)$ / nm	$u_r(a_0)$/ ppm	Comments
Reproducibility upon change of antennas or underestimate of perturbation from loop probes	21	0.23	section 3.1
Upper limit to thickness of a possible dielectric layer on resonator surface	15	0.17	
Estimate of surface resistivity	10	0.11	section 3.2
Total (quadrature sum) a_0	23.2	0.26	
Total squared radius a_0^2		**0.52**	

The absence in Table 2 of relevant uncertainty contributions from the extrapolation of microwave data to zero pressure, or from the discrepancies among the corrected data of several modes, demonstrates the remarkable validity of the perturbation model for the modes other than TM11. The different response of the mode TM11, which is inherent to its peculiar interaction with the electrical properties of the cavity boundary, is a major limiting factor to a further reduction of the uncertainty of a microwave determination of the mean volume of the cavity.

4 . Determination of the speed of sound in helium

4.1 Acquisition and fitting of acoustic data

At each pressure along the experimental isotherm we determined the resonance frequencies $f_{(0,\,n)}$ and the halfwidths $g_{(0,\,n)}$ of nine radial acoustic modes (0,2) to (0,10) by fitting the complex voltage data recorded from the detector microphone while the frequency of the signal fed to the source microphone was swept over the range $f_N \pm 3g_N$ in 22 discrete steps, where f_N and g_N are approximate estimates of $f_{(0,\,n)}$ and $g_{(0,\,n)}$. The fitting function included a quadratic background term, as in eq. (7) in [15], to account for the influence of neighbouring modes in the acoustic spectrum. By comparison with the fitting results obtained with a linear background, the inclusion of the quadratic term was found to be statistically significant for the majority of the modes and particularly at low pressure, as expected by the increase of the resonance halfwidths. In a number of tests with alternative measurement protocols, by reducing or increasing the swept frequency interval and the number of points, and repeating sweeps by first increasing and then decreasing frequency, the fitted parameters remained consistent within the fitting uncertainty estimated by the covariance matrix.

The fitting uncertainty increases at low pressure ($\propto p^{-2}$) due to the combined effect of the reduction in the S/N ratio and the broadening of the resonances. The final type A uncertainty associated to the resonance frequency of each mode was the standard deviation of 24 repeated acquisitions at each pressure (Figure 16), which varied between a relative minimum of 0.1 ppm and a maximum of 1 ppm, depending on the mode, the pressure and the polarization voltage of the detector microphone. These uncertainties were used as weights in the final fits of the acoustic data to zero pressure (Section 4.3).

In principle, the frequency dependence of the halfwidths in the fitting function requires an additional correction to the fitted parameters $f_{(0,\,n)}$ and $g_{(0,\,n)}$ of the order Q_N^{-2} [39]. In practice, the maximum relative value of this correction for mode (0, 2) is 0.08 ppm at 60 kPa and 0.02 ppm at 170 kPa, with a negligible impact on our final determination of the speed of sound at zero pressure.

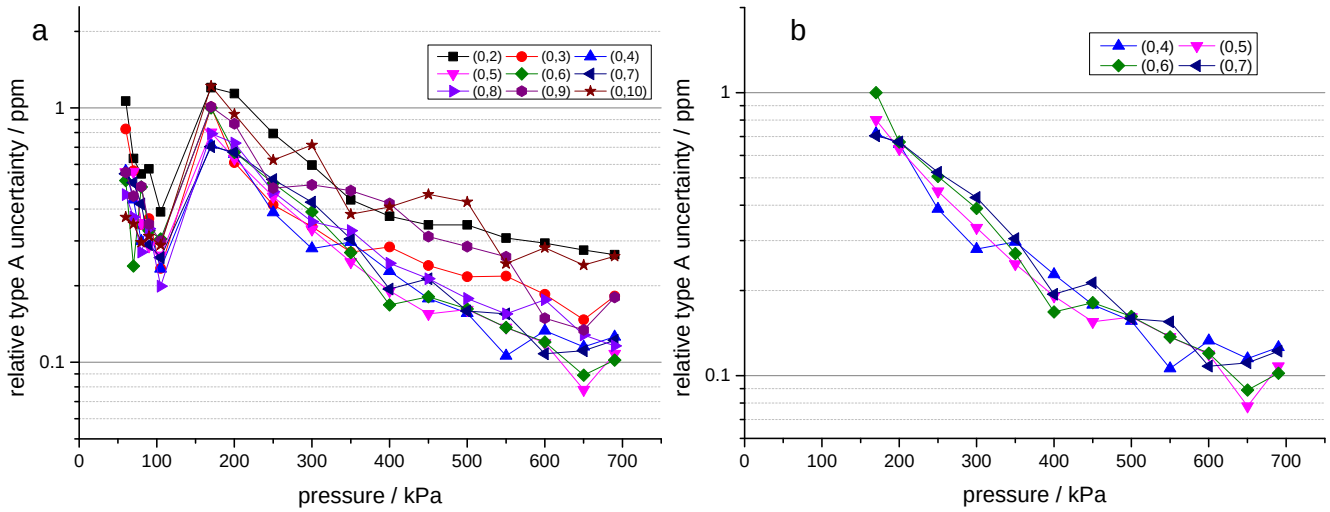

Figure 16. (a) Relative fitting uncertainty for the resonance frequency of modes (0,2) to (0,10) as a function of pressure. The discontinuity below 105 kPa is due to the change of the detector microphone polarization voltage from 28 V to 200 V; (b) Relative fitting uncertainty for the data subset which was selected for the current estimate of R and k; the selection includes four modes (0,4) to (0,7) between 170 kPa and 690 kPa.

4.2 Acoustic model

In this section we illustrate the corrections which were applied to the experimentally measured acoustic frequencies $f'_{(0,n)}$ to determine their corresponding unperturbed values $f^{0}_{(0,n)}$

$$f^{0}_{(0,n)} = f'_{(0,n)} + \sum \Delta f_{(0,n)} \,, \tag{15}$$

as needed to calculate experimental values the speed of sound in helium for each mode at each pressure

$$u_{(0,n)} = 2\pi a \frac{f^{0}_{(0,n)}}{z_{(0,n)}} \,, \tag{16}$$

where a is our microwave estimate (4) of the mean cavity radius and the eigenvalues $z_{(0,n)}$ are determined by our interpretation of the geometry of our cavity (sections 3.3, 4.2.3).

Figure 17 compares the values $u^2_{(0,n)}$ determined from our experimental data for 9 radial acoustic modes with a reference function of pressure u^2_{ref} (p, 273.16 K) which assumes M_{ref} = 4.002602 g mol^{-1} [40], R_{ref}= 8.3144621 J mol^{-1} K^{-1} [16], γ_0 = 5/3 and T = 273.16 K, and calculated values of the density and the acoustic virial coefficients of helium [31, 32].

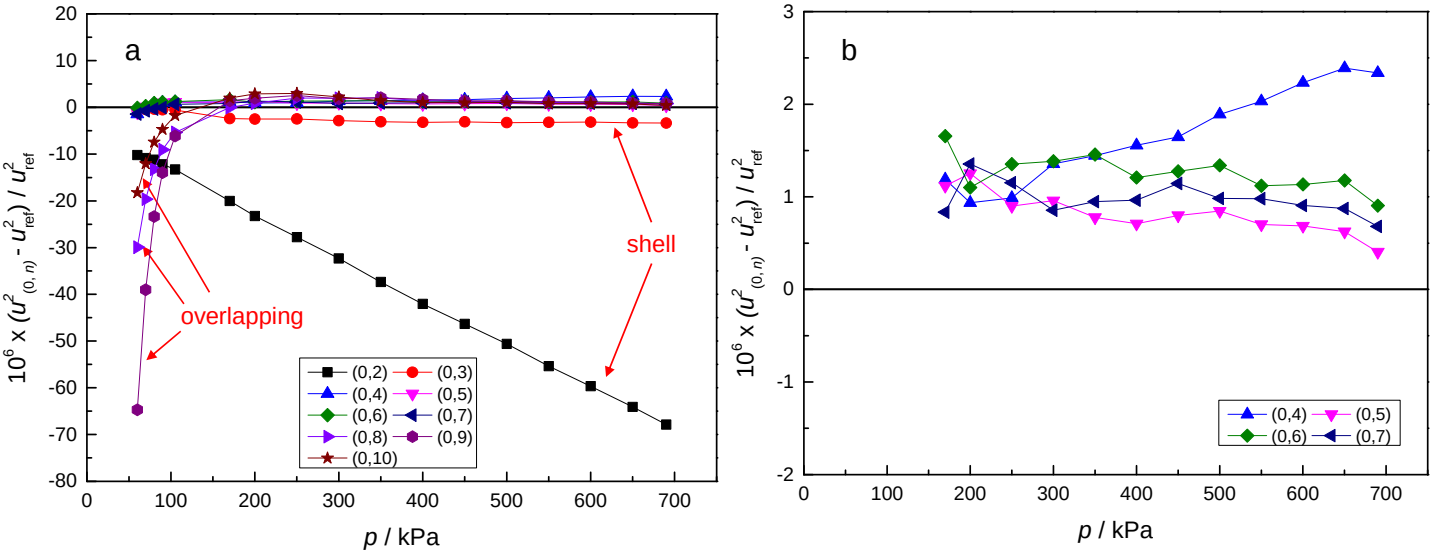

Figure 17. (a) Relative deviations of the squared speed of sound in helium determined from the experimental data of 9 radial modes from a reference function $u^2_{\mathrm{ref}}(p)$. Anomalous deviations for certain modes and pressure ranges are evidenced by text labels and arrows according to their interpretation; (b) Relative deviations of the squared speed of sound in helium from a reference function $u^2_{\mathrm{ref}}(p)$ for the data subset which was selected for the current estimate of R and k; the selection includes four modes (0,4) to (0,7) between 170 kPa and 690 kPa.

In our model, the sum in (15) has contributions from the thermal boundary layer, the coupling of radial acoustic modes within the cavity with a radial elastic mode in the shell, and the finite impedance of three ducts and two microphones (online supplement). In most cases, these frequency perturbations are accompanied by energy losses which contribute to the resonance half-widths $g_{(0,n)}$. Additional contributions to $g_{(0,n)}$ are given by thermo-viscous losses in the bulk of the fluid and by second-order corrections to heat exchange in the thermal boundary layer [41]. All these contributions are used to calculate an estimate of the half-widths $g^{c}_{(0,n)}$. Then, the adequateness of our model can be verified by the agreement of $g^{c}_{(0,n)}$ with our experimental estimate of the same quantities. Figure

18 illustrates this comparison displaying the relative excess half-widths $2(g_{(0,n)} - g^{c}_{(0,n)}) / f_{(0,n)} = 2\Delta g_{(0,n)} / f_{(0,n)}$.

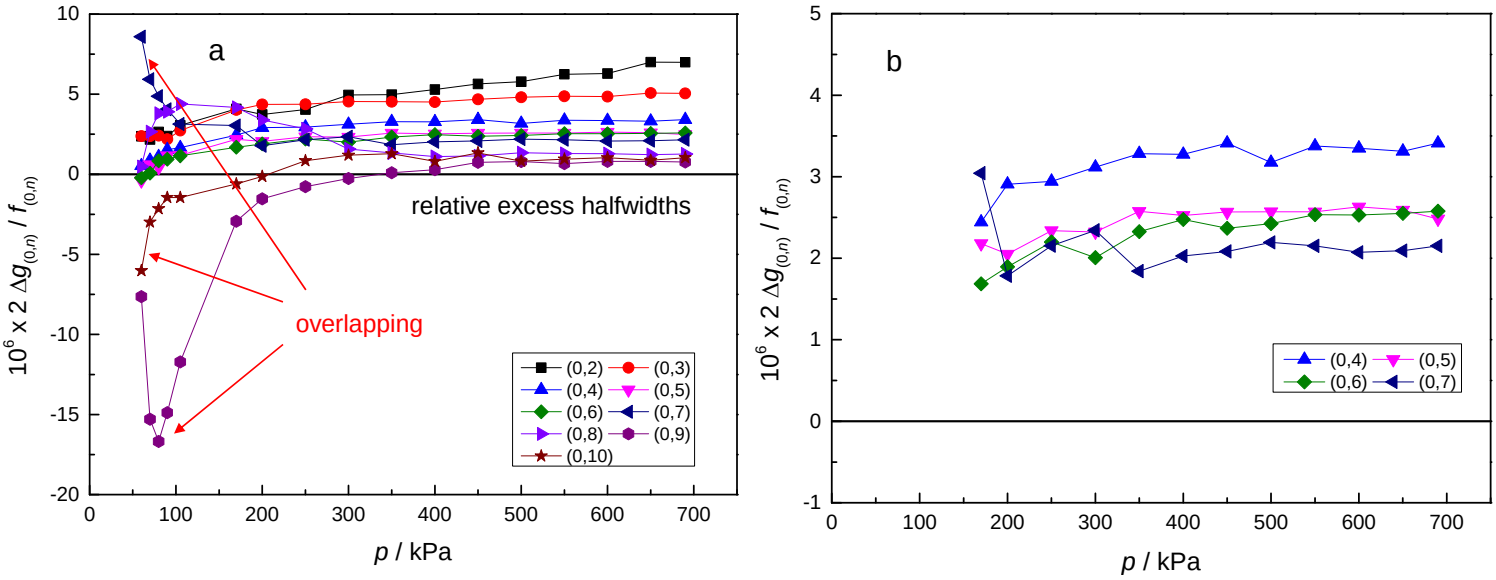

Figure 18. (a) Double relative excess half-widths for 9 radial modes in the pressure range 60 kPa to 690 kPa. Anomalous excessive and defective energy losses for certain modes and pressure ranges are identified by text labels and arrows according to their interpretation; (b) Double relative excess half-widths for the data subset which was selected for the current estimate of R and k; the selection includes four modes (0,4) to (0,7) between 170 kPa and 690 kPa.

The comparison of figures 17 and 18 highlights the limits in the validity of our model and indicates that only a subset of the investigated modes may be used for the sake of an accurate determination of R and k. Particularly, the corrected frequency (and speed of sound) data of the (0,2) and (0,3) modes show relevant systematic differences from the other modes over the whole investigated pressure range; for mode (0,2) these differences increase linearly as a function of pressure. These same modes are also characterized by the largest excess half-widths in the dataset. Most likely, these features are a consequence of the vicinity with the breathing mode of the shell, which is calculated (section 4.2.3) at a frequency which is intermediate between that of modes (0,2) and (0,3). Both the frequencies and the half-widths of the high frequency modes (0,8), (0,9) and (0,10) show non-linear convoluted deviating trends at low pressure. Also, the half-width of mode (0,7) shows an anomalous increase below 100 kPa. As reported in previous work with helium [6, 42] these anomalous trends are a consequence of the overlap from neighboring nonradial modes in the acoustic spectrum. Due to the elevated number of components in these multiplets, with different associated amplitudes and phases, the consequences of overlapping are extremely hard to predict, apart from the general expected features that these effects will increase proportionally to p^{-2}, due to increase of the mode half-widths, and that the combination of phases within the single components of the multiplets may result, depending on the mode and the pressure in an increase, or a decrease of the frequency and half-width of neighbouring radial modes.

The previous observations motivate our choice of a subset of the acoustic data comprising 4 radial modes (0,4), (0,5), (0,6) and (0,7) over the limited pressure range between 170 kPa and 690 kPa to preserve the accuracy of our determination of R and k.

To highlight the limits of our model, in figure 19 we anticipate the residuals of a single global fit to our selected acoustic data as a function of pressure using eq. (5). This plot is equivalent to a magnification of figure 17 b, upon changing the reference function of the comparison from u^2_{ref} to

$\langle u^2_{\mathrm{fit}} \rangle$. Remarkably, the fractional residuals span an interval of about ±1.2 ppm at 690 kPa, decreasing to ±0.5 ppm at 170 kPa. However, particularly at high pressure, where precision is comparatively better and many of the corrections in (16) are larger, it is evident that the residuals are not randomly distributed and are clearly mode dependent. The amplitude of these systematic differences are an estimator of our limited understanding of the perturbations to the acoustic eigenfunctions.

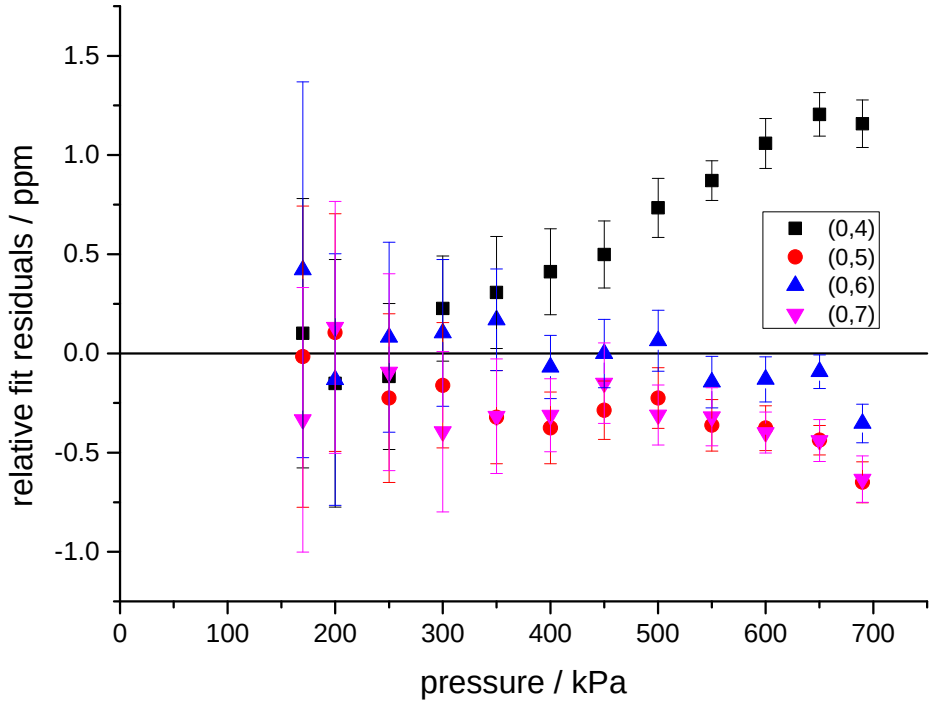

Figure 19. Residuals of a linear combined fit with (18) to selected acoustic data for 4 radial modes in the pressure range 170 kPa to 690 kPa. The error bars display the type A fitting uncertainty of each single datum previously showed in Fig. 16 b.

As a second estimator of this limit, we considered the zero pressure limit obtained by fitting the relative excess half-widths $2\Delta g_{(0,n)} / f_{(0,n)}$ with a quadratic function of the pressure, i.e. the same function which is used to interpolate the squared acoustic frequencies. The intercept of these fits was 0.58 ppm for mode (0,4), 0.14 ppm for mode (0,5), − 0.12 ppm for mode (0,6). For mode (0,7) this estimator is biased at low pressure by the deviating trend caused by overlapping with mode (13, 2). Finally, in figure 20 we plot the functions $2\Delta g_{(0,n)}/(g_{(0,n)} f_{(0,n)})$, which accounts for the increase of the

half-widths at low pressure which is driven by thermal boundary layer losses. We positively interpret the trend to zero as an indication of the absence of relevant flaws in the acoustic model at low pressure.

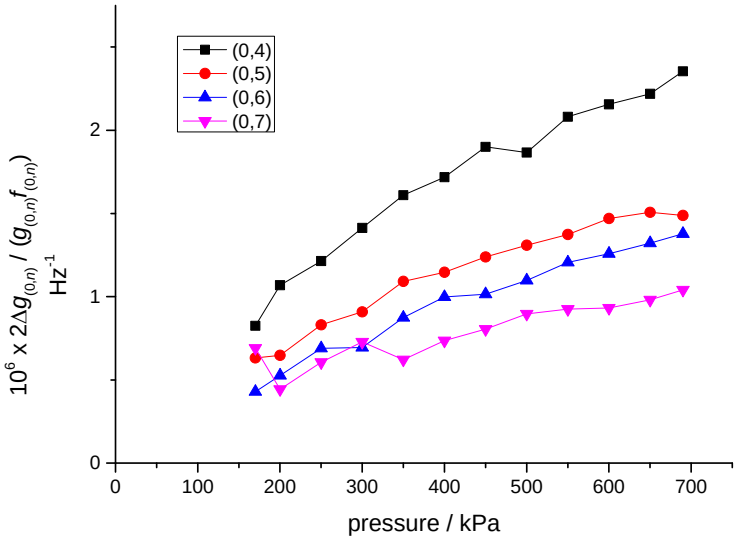

Figure 20. Excess half-widths of modes (0,4) to (0,7) scaled by $10^6 / (g_{(0,n)} \times f_{(0,n)})$.

4.2.1 Boundary layer correction. The theory of the interaction of acoustically driven gas motion in a boundary layer near the cavity wall is well established [43]. For the radial modes and the pressure range of interest in this work the relative perturbation to the resonance frequencies varies between a minimum of –54 ppm for mode (0,7) at 690 kPa and a maximum of –148 ppm for mode (0,4) at 170 kPa, representing the largest correction to the experimental frequencies and the largest contribution to the half-widths. The uncertainty associated to the calculation of this correction is small because of the recent improvements in the theoretical calculation of the thermophysical properties of helium [31], which predict $\lambda_{\mathrm{He}} = (146.0349 \pm 0.0014)$ mW m^{-1} K^{-1} for the thermal conductivity of helium at 273.16 K and zero pressure, with a negligible (< 0.01 ppm) impact on our determination of the squared speed of sound in helium u_0^2. The thermal boundary layer correction also depends on pressure (or density) in a two-fold way: i) by the pressure dependence of the density and the isobaric heat capacity of the gas in the thermal penetration length; ii) by the density correction $\mathrm{d}\lambda/\mathrm{d}\rho$ of the thermal conductivity, with different literature sources [6, 44, 45] providing variable estimates of this parameter in the range (0.36 ± 0.07) mW m^2 K^{-1} Kg^{-1}. To assess the contribution of these two sources to the overall uncertainty of u_0^2, we have changed the value of λ_{He} and p by their estimated standard uncertainty and repeated the final fit to our acoustic data (section 4.3), with the resulting contributions reported in Table 4.1.

4.2.2 Thermal accommodation. The imperfect accommodation of temperature at the interface between the gas and the cavity wall leads to a correction of the frequencies of an acoustic resonator [46] which is particularly important at low pressure. This correction is a non linear function of pressure, increasing as p^{-1}, so that a suitable term must be added to the acoustic virial expansion (5) used for the final fit of $u^2(p)$ to cancel out its effect on u_0^2. When this is done to the present data, as recorded in July 2014, for the selected set of modes (04, 05, 06) which were found in better agreement with the perturbation model (15) over the whole pressure range between 60 kPa and 690 kPa (figure 18), we obtain $h_{\mathrm{July}} = (0.410 \pm 0.004)$. Unfortunately, this estimate is not consistent with a previous result $h_{\mathrm{March}} = (0.389 \pm 0.006)$ obtained from the analysis of acoustic data recorded in March 2014 in the same experimental conditions. While we do not have a convincing explanation for this inconsistency, we note that previous experimental estimates of the thermal accommodation coefficient h for helium in contact with copper vary between a minimum of (0.38 ± 0.01) [42] and a maximum of (0.41 ± 0.01) [47]. Recently, an extremely precise estimate $h = (0.393 \pm 0.001)$ was reported [5] for helium in contact with a surface of electrolytic copper with the same finishing as that of the cavity used in this work. Previous work also demonstrated that h, or the strictly related momentum accommodation coefficient are extremely sensitive to the nature of the surface of the cavity wall, and particularly to the adsorbed layer of molecules [48], so that an independent (obtained from a different apparatus) estimate of h can not safely be assumed for the calculation of the correction needed in this work. In principle, the inconsistency between our two values h_{March} and h_{July} may reveal a time-dependent variation of the condition of the surface of our cavity. However, a closer observation (Figure 21) to the results of the fitting procedures which led to our estimates of h reveals that the residuals of the July data are increasingly deviating at the lowest pressures, a trend that was absent from the data recorded in March, seemingly more reliable. These observations drive our final choice for a mean value of the thermal accommodation coefficient $h = (h_{\mathrm{March}} + h_{\mathrm{July}})/2 = (0.399 \pm 0.015)$, where the conservative estimate of the uncertainty encompasses all the discrepant estimates and results discussed above. The relative contribution of this uncertainty to our final determination of u_0^2 is 0.43 ppm, as reported in table 3.

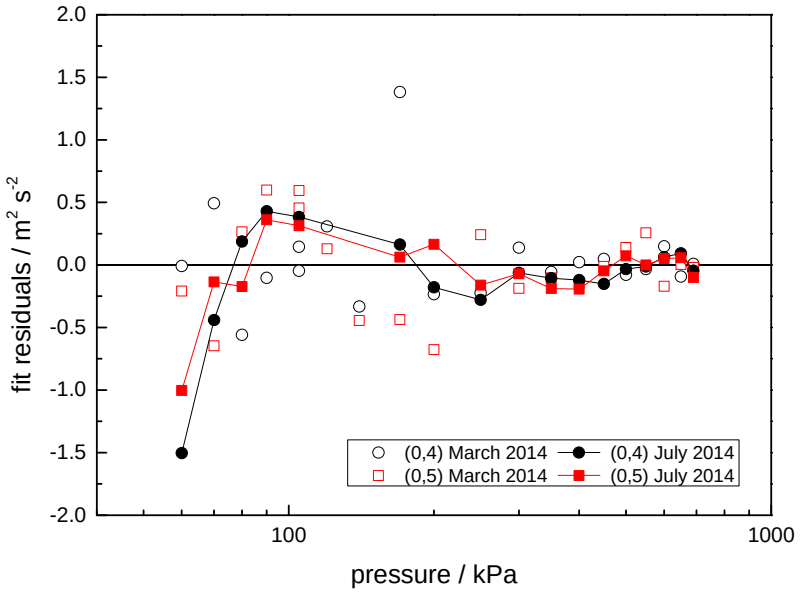

Figure 21. Fit residuals from interpolations with equation $u^2(p) - A_2 p^2 = A_{-1} p^{-1} + u_0^2 + A_1 p$ of two different acoustic datasets: March 2014 (hollow symbols); July 2014 (full symbols). These interpolations lead to inconsistent estimates of the thermal accommodation coefficient: $h_{\mathrm{March}} = (0.389 \pm 0.006)$ and $h_{\mathrm{July}} = (0.410 \pm 0.004)$. The low-pressure deviating trend of the residuals of the July dataset indicates that the latter estimate of h is not reliable.

4.2.3 Shell coupling. Using a classical model [49] for the acoustic admittance of our shell and tabulated values for the density and the elastic properties of copper we initially calculated the breathing mode frequency f_{br} = 10.63 kHz. Successively, we refined our estimate of this parameter by fitting the mode-dependent acoustic slopes ($\propto p$) of acoustic data, previously corrected for the thermal boundary layer, as measured in helium and in argon (from an additional available dataset) with the result $f_{br} = (10.0 \pm 0.1)$ kHz, where the reported uncertainty spans different estimates obtained by imposing different combination of fitting constraints on the elastic compliance of the shell and the second acoustic virials of helium and argon. We then used this refined estimate of f_{br} to calculate shell corrections $\Delta f_{(0,n)} / f_{(0,n)}$ using the simplified model

$$\left(\frac{\Delta f_{(0,n)}}{f_{(0,n)}}\right)_{\text{shell}} = \frac{-\gamma p\left(\chi_{\text{int}}/3\right)}{1-\left(f_{(0,n)}/f_{\text{br}}\right)^2}, \tag{17}$$

where $\chi_{\text{int}} = 4.68 \times 10^{-11}$ Pa^{-1} is the compliance of the shell to an increase in the internal pressure. Figure 22 shows the effect of applying these corrections to our acoustic data in helium. It is evident from the residual slope of mode (0,2), and to a much lesser extent of mode (0,3), that the simplified model (17) does not properly and fully account for shell coupling with these modes; however, the model drastically reduces the relative dispersion of modes (0,4) to (0,10) and eliminates the discrepancy from their expected pressure slope $u_{\text{ref}}(\beta_a/RT)^{0.5}$. The applied frequency corrections are a linear function of pressure, so their application does not change and does not contribute to the uncertainty of our final determination of u_0^2.

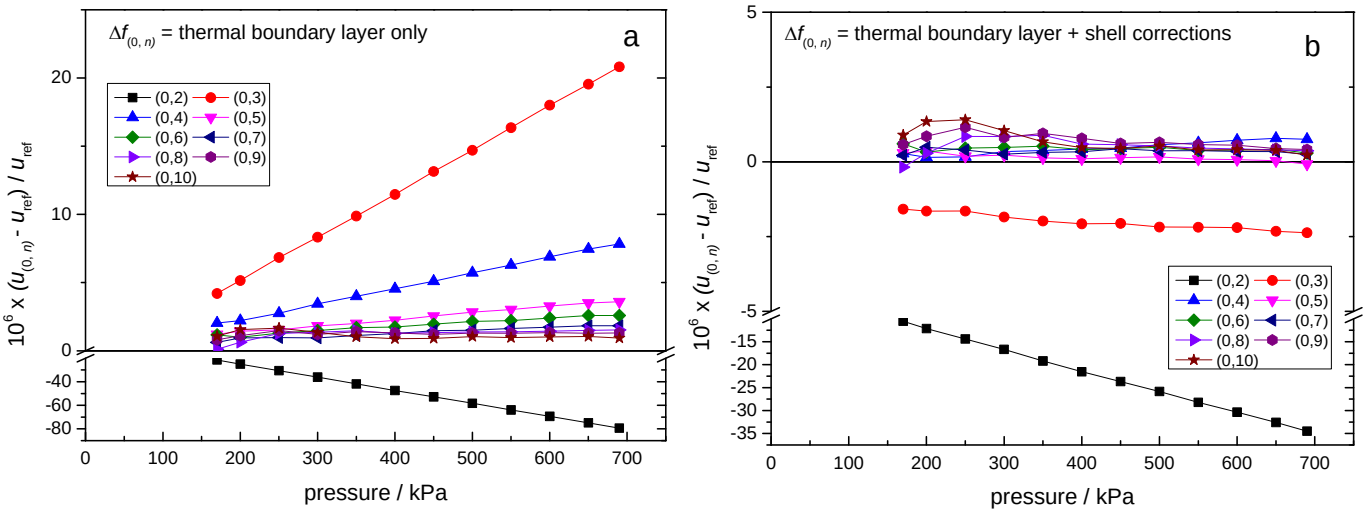

Figure 22. Relative deviations of the speed of sound in helium determined from the experimental data of 9 radial modes from a reference function $u_{\text{ref}}(p)$: (a) after applying corrections for thermal boundary layer effects only; (b) after applying corrections for thermal boundary layer and coupling with a radial elastic mode in the shell.

4.2.4 Geometrical correction. Based on our microwave interpretation (section 3.3) of the cavity geometry as being suitably described by an ellipsoid with semi-axes defined by two shape parameters $\varepsilon_1 = 1.97 \times 10^{-4}$, $\varepsilon_2 = 1.02 \times 10^{-4}$, we used the perturbation model for the acoustic radial modes of a triaxial ellipsoid [50] to calculate appropriate geometrical corrections to the acoustic eigenvalues. The relative difference of the corrected eigenvalues from those of a perfect sphere varies between 0.017 ppm for $z_{(0,2)}$ and 0.77 ppm for $z_{(0,10)}$ (online supplement). If, alternatively, the geometrical correction

would not be applied to the microwave and the acoustic eigenvalues, our estimate of u_0^2 would be found to vary by 0.15 ppm. We account for the possible error associated to treating our misaligned cavity as an ellipsoid with an uncertainty contribution (table 3) equal to half of this variation, i.e. 0.08 ppm.

4.2.5 Acoustic perturbation from ducts and microphones. The input acoustic admittance of the three ducts illustrated in figure 7 was calculated using a method based on transmission line theory [51]. The overall relative perturbation to the real and imaginary parts of the eigenfrequencies of modes (0,4) to (0,7) of our AGT is illustrated in figure 23. As a first estimator of the uncertainty associated to the ducts corrections we repeated the calculation of the acoustic impedance of the ducts using an alternative method [52]. The compared relative differences between the predictions of these two methods was found to be always less than 0.05 ppm. As a second estimator of the possible error associated with the ducts corrections, we considered the variation in the perturbations induced by slight changes (± 5%, ± 10%) of the radius and length of the various sections comprising each duct. The gas outlet duct was found to be most sensitive to these changes, with corresponding variations of the relative frequency perturbation as large as 0.1 ppm. We finally account for the possible error of the duct correction with an uncertainty contribution to u_0^2 of 0.12 ppm.

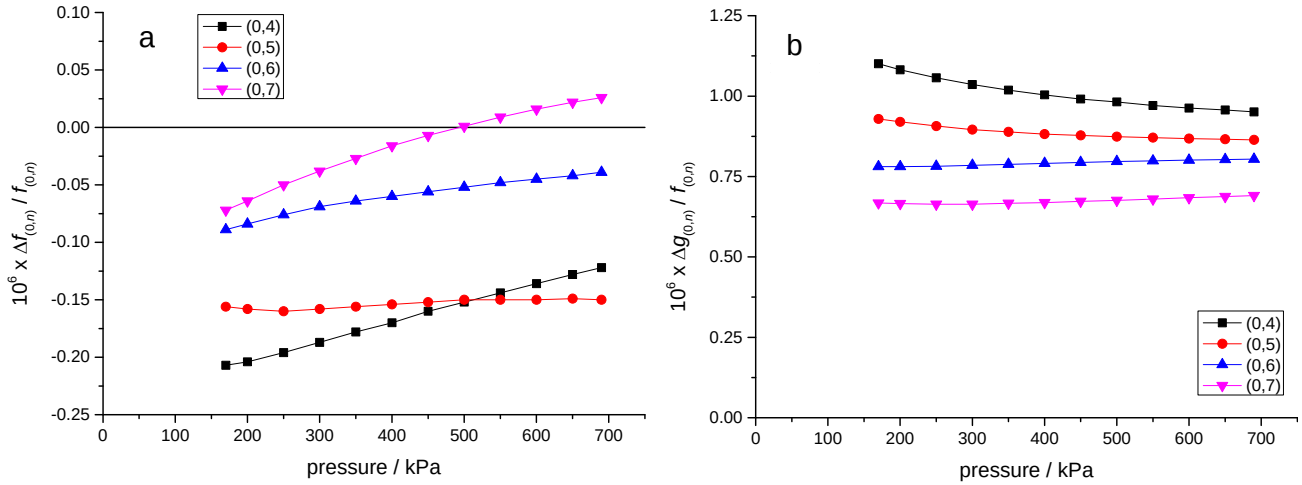

Figure 23. Perturbing effect due to the finite impedance of the three ducts sketched in figure 7 on the modes (0,4) to (0,7) between 170 kPa and 690 kPa: (a) relative frequency perturbations; (b) relative contribution to the half-widths.

The frequency shifts and the contribution to the half-widths due to the finite acoustic impedance of two acoustic transducers (1/4-inch free-field condenser microphones) were calculated using the procedures and the model in [53] with the results displayed in figure 24. To estimate an uncertainty contribution for these corrections, we varied those structural parameters of the microphones to which the impedance is most sensitive, i.e. the membrane tension which was varied by ± 10% and the

volume of the backing-cavity which was varied by ± 30%; we found that the relative frequency corrections induced by any combination of these changes was always less than 0.05 ppm.

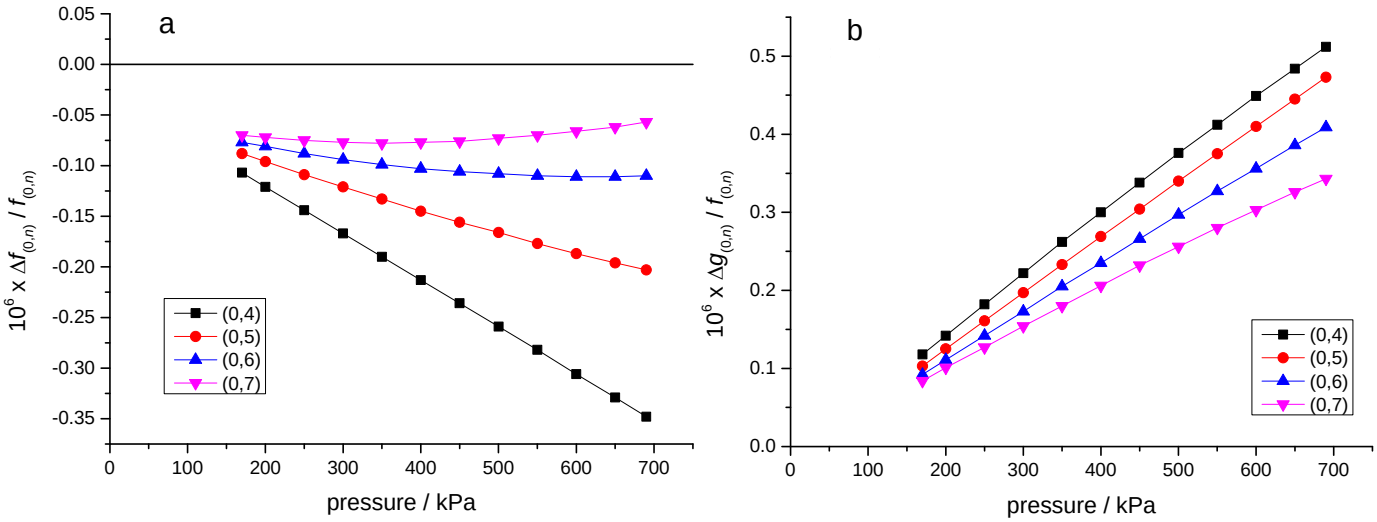

Figure 24. Perturbing effect due to the finite impedance of two microphones on the modes (0,4) to (0,7) between 170 kPa and 690 kPa: (a) relative frequency perturbations; (b) relative contribution to the half-widths.

4.3 Isotherm analysis and final acoustic results

We estimate the speed of sound in helium at zero pressure, 273.16 K, $u_0^2 = (945\,710.45 \pm 0.41)$ m^2 s^{-2} by a single fit of combined acoustic data for modes (0,4) to (0,7) to the following linear function of the pressure between 690 kPa and 170 kPa:

$$u^2(p) - A_{-1}p^{-1} - A_2p^2 = u_0^2 + A_1p, \qquad (18)$$

where $A_{-1} = 1.865 \times 10^6$ m^2 s^{-2} Pa is constrained by our choice of the thermal accommodation coefficient $h = 0.399$ (section 4.2.2), and $A_2 = 2.86 \times 10^{-12}$ m^2 s^{-2} Pa^{-2} is constrained by assuming the value of the third acoustic virial coefficient of helium $RT\gamma_a = (15.61 \pm 0.88)$ cm^6 mol^{-2} from theory [32]. The opportunity of the latter assumption relies on the observation that when A_2 is left as a free parameter in fitting (18), it is found to be not significantly different from zero: $A_2^{fit} = (0.36 \pm 4.91) \times 10^{-12}$ m^2 s^{-2} Pa^{-2}, as a consequence of the limited pressure range investigated in this work. If we assumed $A_2 = 0$, our determination of u_0^2 would decrease by 0.58 ppm, which is about half the standard error of our determination of R and k. To perform the interpolation (18), each single datum for each mode at each pressure was inversely weighted by the square of its estimated standard deviation (figure 16 b). From the fitted value of $A_1 = (9.2521 \pm 0.0007) \times 10^6$ m^2 s^{-2} Pa^{-1}, we deduce our experimental estimate of the second acoustic virial coefficient of helium at 273.16 K: $\beta_a^{Exp} = (22.2195 \pm 0.0017)$ cm^3 mol^{-1} , in remarkable agreement with the theoretical estimate of the same quantity $\beta_a^{th} = (22.2202 \pm 0.0013)$ cm^3 mol^{-1} [31].

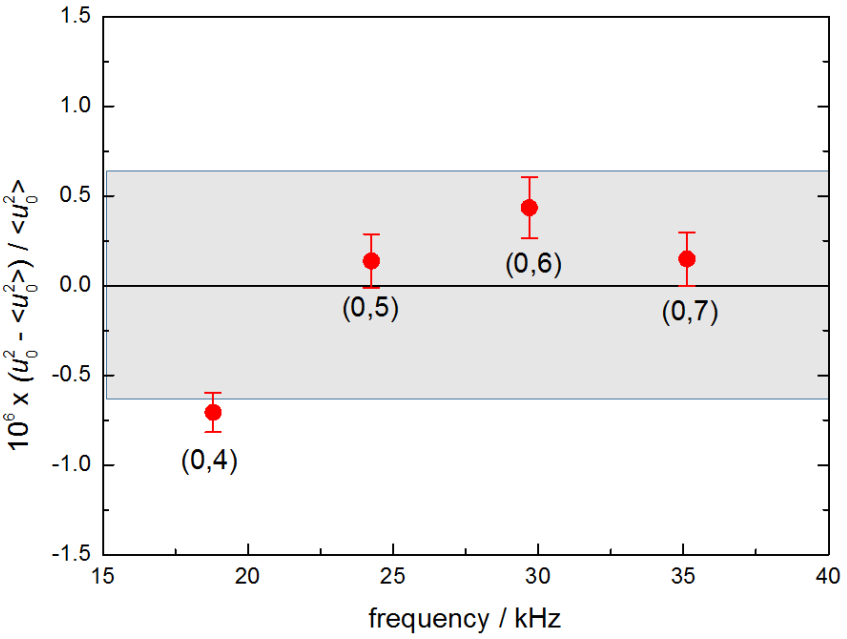

Figure 25. Relative differences of the results of separate fits to the acoustic data of each mode from the mean result of a combined fit to all modes with (18). The uncertainty bars display the fitting uncertainty of each mode. The grayed rectangular area corresponds to our inflated estimate (± 0.57 ppm) of the uncertainty of our acoustic model.

The residuals of the combined fit with (18), previously displayed in figure 19, evidenced small but clear mode-dependent systematics. To provide an alternative quantitative estimate of these effects we repeated the fit with eq. (18) to the acoustic data of each mode separately with the results displayed in figure 25. The relative dispersion of these mode-dependent determinations of u_0^2 spans the range between −0.71 ppm and 0.43 ppm with respect to the result of the combined fit $< u_0^2 >$. We assume one half of the dispersion interval (0.57 ppm) as an uncertainty contribution conservatively representative of the discrepancy among different modes, i.e. representative of the imperfectness of our acoustic model.

The present estimate of u_0^2 is based on the analysis of a significantly restricted dataset which excludes several modes and all the low-pressure data below 170 kPa. As discussed in section 4.2, we believe that such significant data rejection has a firm justification. However, for the sake of evaluating whether our final assessment of the uncertainty of u_0^2 is adequate, we now discuss the consequences of alternative choices of the final dataset. Firstly, we consider the consequences of enlarging the number of modes while maintaining the restriction of the pressure range (170 kPa to 690 kPa): i) a combined fit to seven radial modes, (0,4) to (0,10) increases u_0^2 by 0.65 ppm; ii) if the mode (0,3) is additionally included, the relative increase with respect to the same reference is 0.14 ppm. Secondly, we consider the consequences of including low-pressure data, covering the overall pressure interval between 60 kPa and 690 kPa: i) a combined fit to our original choice of the four radial modes (0,4) to (0,7) brings a relative change of u_0^2 by −0.31 ppm; ii) the additional inclusion of mode (0,3) brings a relative change of u_0^2 by −0.55 ppm. All these alternative results are consistent with our original estimate of u_0^2 within the combined standard uncertainties. Predictably, due to shell coupling and overlapping with neighbouring modes (figures 17 and 18), the inclusion in these tests of the (0,2) mode or the low-pressure data for modes (0,8) to (0,10) do not represent reasonable options, due to the large systematic residuals which lead to a dramatic increase of the associated fitting uncertainty.

Finally, the various contributions to the overall uncertainty of our determination of the squared speed of sound in helium are summarized in table 3.

Table 3. Uncertainty budget for squared speed of sound in helium at zero pressure, 273.16 K

Source	$u(u_0^2)$ / m^2 s^{-2}	$u_r(u_0^2)$ / ppm	comments
Dispersion of four radial acoustic modes	0.54	0.57	section 4.3
Squared microwave radius	0.49	0.52	section 3.6
Thermal accommodation coefficient h	0.41	0.43	section 4.2.2
Thermal conductivity of helium	0.02	0.03	section 4.2.1
Pressure constant offset (10 Pa)	0.09	0.10	section 2.6
Geometrical correction	0.07	0.08	section 4.2.4
Ducts correction	0.10	0.11	section 4.2.5
Microphone correction	0.05	0.05	
Total (quadrature sum) u_0^2	**0.85**	**0.90**	

5. Estimate of the molar mass of helium

The choice of using helium as the working gas for AGT requires a careful assessment of the possible presence of contaminants in the test sample, including trace amounts of inert gases other than helium. In this work, our final estimate of the molar mass of the working gas relies on the results of precise mass spectrometric analyses (section 5.1) for three different samples: i) a sample of helium, denoted 7L purchased from Linde AG. This sample was analyzed to determine the isotopic ratio $^3He/^4He$ and the concentration of inert gas impurities; ii) a sample of helium purchased from Messer-Griesheim, denoted MG1, which was used for a preliminary determination of the speed of sound in our apparatus. This sample was analyzed to determine the abundances of several possible impurities including inert gases other than He, water vapor and other common contaminants; iii) a sample of helium purchased from Messer-Griesheim, denoted HeMG2, which was used for the speed of sound measurements presented and discussed in this work. This sample underwent the same type of analysis as HeMG1, and is seemingly even purer.

The speed of sound in these three samples were compared in our apparatus at the reference pressure of 105 kPa, 273.16 K (section 5.2). Within their limited precision, the results of these comparative tests were consistent with the results of the mass spectrometric analyses.

To minimize the possible contaminating effect due to outgassing or virtual leaks, acoustic measurements were conducted while continuously purging helium through the internal volume of the resonator at the large flow rate of 7.5×10^{-5} mol s^{-1} (100 sccm). In section 5.3 we describe a test made to obtain a quantitative estimate of the possible influence of outgassing in our experimental conditions. Our final estimate of the molar mass of our working sample and its associated uncertainty is discussed in section 5.4.

5.1 Mass spectrometric analyses

As noted previously for argon [3, 4, 6], the variation of the isotopic composition of helium is expected to have a minor impact on the uncertainty of an absolute AGT. The origin of commercially-produced He is from the natural accumulations of ^4He rich gas in the continental crust, rendering the isotopic ratio $\mathfrak{R}$ in bottled He significantly lower than its reference value in air $\mathfrak{R}_{atm} = (^3He/^4He)_{atm} = (1.37 \pm 0.03)$ μmol mol^{-1} [40]. Assuming atmospheric composition leads to an underestimate of M, due to the different origin of commercial samples [20]. To support this statement, in table 4 we list the results of mass spectrometric analyses that include the determination of $\mathfrak{R}$ of one sample of helium previously used at INRiM - 7L - from two different laboratories: i) Linde AG Central Analytics (LAG); ii) the Scottish Universities Environmental Research Centre (SUERC). In spite of their being inconsistent, with $\mathfrak{R}_{LAG} = (0.38 \pm 0.02)$ μmol mol^{-1} and $\mathfrak{R}_{SUERC} = (0.26 \pm 0.01)$ μmol mol^{-1}, both analyses indicate that the determined $^3He/^4He$ ratio for L7 is significantly lower than the natural abundance in air. Concentrations of residual noble gases are low (Table 4).

Gas impurities in the helium are likely a larger contribution to speed of sound measurement than the He isotope composition. For the speed of sound measurements, helium was simply drawn from the source cylinders and purified by passing through a heated zirconium aluminum getter (SAES Getter PS2 GC50-R) designed to reduce reactive gas impurities like O_2, H_2O, CO, CO_2, H_2, CH_4 and N_2 to low parts per billion (ppb) levels or below, when operated within its maximum flow rate specification of 1.5×10^{-4} mol s^{-1} (200 sccm). In a preliminary test, we alternatively routed the gas flow through the getter, or through a by-pass branch of the manifold (figure 9), to test the possible level of reactive gas impurities and estimate the effectiveness of the getter. Based on the comparison of the resonance frequencies of 4 radial acoustic modes of our resonator, this test produced a relative mean variation of the frequency of the modes by (-1.03 ± 0.02) ppm when the getter was by-passed. This could be caused by 0.5 ppm of H_2O, 0.32 ppm of N_2, or 0.2 ppm of CO_2.

Table 4. Results of mass spectrometric analysis of sample 7L. Bold-typed concentrations refer to levels of impurities measured above the detection limit of the mass-spectrometers

Linde AG Central Analytics			SUERC		
analyte	concentration μmol mol^{-1}	notes	analyte	concentration μmol mol^{-1}	notes
^{3}He	**0.38 ± 0.02**	measured	^{3}He	**0.26 ± 0.01**	measured
Ne	**0.07 ± 0.02**	measured	Ne	< 1.25	detect. limit
Ar	**0.09 ± 0.02**	measured	Ar	< 4.17	detect. limit
Kr	**0.003 ± 0.001**	measured	Kr	< 0.008	detect. limit
Xe	< 0.03	detect. limit	Xe	< 0.002	detect. limit

In order to sample working gases for the identification of impurities we realized a collecting system comprising an auxiliary manifold composed by all-metal parts (gaskets, fittings, valves), 1/4-inch and 1/8-inch tube sections with electropolished internal surfaces and stainless steel gas cylinders of 1 litre volume with electropolished internal surface. The manifold was evacuated and the sampling cylinder baked (at 160 °C) for several days until the residual pressure reading from a Penning vacuum gauge was less than 5×10^{-5} Pa (5×10^{-7} mbar). At this point the inlet valve of the cylinder was closed and the cylinder left to cool back to ambient temperature. The cylinder was then connected to the main experimental manifold at a sampling point (figure 8) located downstream from the heated getter and upstream from the internal volume of the resonator. The sampling cylinders were filled up to 1.5 MPa by flowing at 100 sccm. We assume that the composition of the sampled gas at this point is representative of the composition of the gas within the resonator in ordinary experimental conditions.

Table 5. Results of PTB mass spectrometric analysis of samples MG1 and MG2. Bold-typed concentrations refer to levels of impurities measured above the detection limit of the mass-spectrometer

MG1			MG2		
analyte	concentration $x \pm u(x)$ μmol mol^{-1}	det. limit μmol mol^{-1}	analyte	concentration $x \pm u(x)$ μmol mol^{-1}	det. limit μmol mol^{-1}
H_2	0.068 ± 0.046	0.300	H_2	0.064 ± 0.028	0.300
CH_4	0.006 ± 0.007	0.020	CH_4	0.003 ± 0.005	0.020
H_2O	0.020 ± 0.030	0.100	H_2O	not detected	0.100
Ne	**0.019 ± 0.006**	0.010	**Ne**	**0.013 ± 0.008**	0.010
N_2 + CO	not detected	0.100	N_2 + CO	0.000 ± 0.000	0.100
O_2	not detected	0.010	O_2	not detected	0.010
Ar	**0.082 ± 0.003**	0.010	Ar	0.008 ± 0.002	0.010
CO_2	0.001 ± 0.003	0.050	CO_2	0.006 ± 0.003	0.050
Kr	0.003 ± 0.002	0.010	Kr	0.002 ± 0.002	0.010
Xe	0.005 ± 0.002	0.010	Xe	0.007 ± 0.003	0.010

Two samples, denoted MG1 and MG2, were prepared at INRiM with this procedure, separated by a few months. The samples were drawn from two different source cylinders supplied from the manufacturer with the same purity specification (Messer-Griesheim 6.0). Within a couple of weeks after their preparation, the samples were analysed by PTB with the same instrumentation previously used for a determination of k by dielectric constant gas thermometry [7]. The gas-handling system

for the inlet of the gas-sample was designed as an ultra-high-purity system using metal gaskets (VCR metal gasket), ultra-high-purity stainless-steel tubing (EN standard number 1.4435/ X2CrNiMo18-14-3), and electro-polished internal surfaces (mean roughness index $R_a \leq 0.25$ µm) in all parts (tubes, valves etc.). The mass spectrometer (GAM 400, InProcess Instruments) is integrated in the gas-handling system. Its mass resolution ranges from 0.5 amu to 2 amu, with a detection limit less than 300 ppb for H_2, 100 ppb for N_2, 50 ppb for CO_2, 20 ppb for CH_4, and less than 10 ppb for most other elements and molecules. The mass spectrometer is equipped with a permanently heated gas-inlet system and a measuring chamber which was baked out for months to minimise water vapour. With this system, a measurement of spectra over at least half an hour, leads to a detection limit of 20 ppb for water. In the present measurements the relatively small sample allows for measurement times of at most 5 minutes, decreasing the S/N ratio. Therefore, a detection limit for water molecules of 100 ppb in the helium samples is a realistic upper limit.

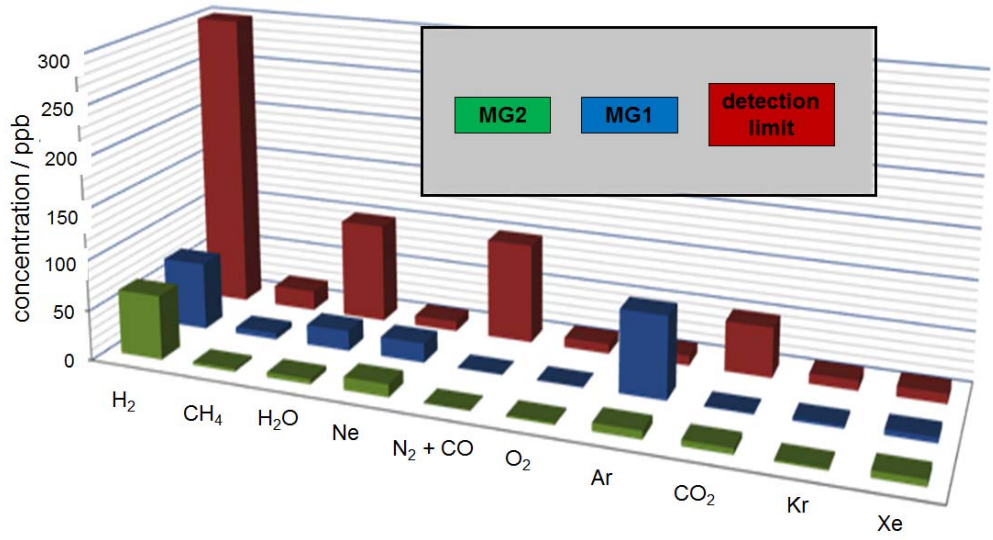

Figure 26. Results of a mass spectrometric analysis of gas impurities in two helium samples made at PTB.

The spectra have been taken using two different methods. The first method is the measurement of spectra with reference to the residual gas in the analysis chamber. This yields correct values for noble gases. The second method is a measurement with reference to highly pure helium (nominal purity of 99.99999 %), as used in [7]. The reference helium was further purified via a purifier (adsorber) MicroTorr SP70 from SAES Pure Gas, Inc., and a helium purifier (getter) HP2 from Valco Instruments, Co. Inc. This second method is helpful for excluding gases desorbed from the inner surface of the chamber. A frequent switching between measuring the gas under test and the reference gas from the gas supply allows for correction of the mass-spectrometer drifts.

The results of these analyses are listed in table 5 and graphically shown in figure 26. For the sample MG1 only two signals were measured above the detection limit, corresponding to small but significant amounts of argon (82 ppb) and neon (20 ppb). For the working gas sample MG2 the only detectable impurity was neon (13 ppb).

5.2 Comparison of speed of sound in different helium samples

From the results of the mass spectrometric analyses summarized in table 5.1 and 5.2, we expect that the squared speed of sound in MG1 and MG2 would be relatively larger than in L7 by 0.35 ppm and 1.10 ppm respectively. These expectations were confirmed by a comparison of the frequency of three radial modes (0,4), (0,5) and (0,6) in the three samples L7, MG1 and MG2 in the same experimental conditions (105 kPa, 273.16 K) which provided the mean estimates $(u^2_{MG1} - u^2_{L7}) / u^2_{L7} = (0.20 \pm$

0.47) ppm and $(u^2_{MG2} - u^2_{L7}) / u^2_{L7} = (1.14 \pm 0.51)$ ppm (figure 27). We take this agreement as the rationale for the assumption $\mathfrak{B}_{MG2} = \mathfrak{B}_{L7} = 0.26 \times 10^{-6}$, with a relative uncertainty contribution of $u_r(M_{MG2}) = 0.17$ ppm (table 6) to conservatively account for the uncertainty of the speed of sound comparison.

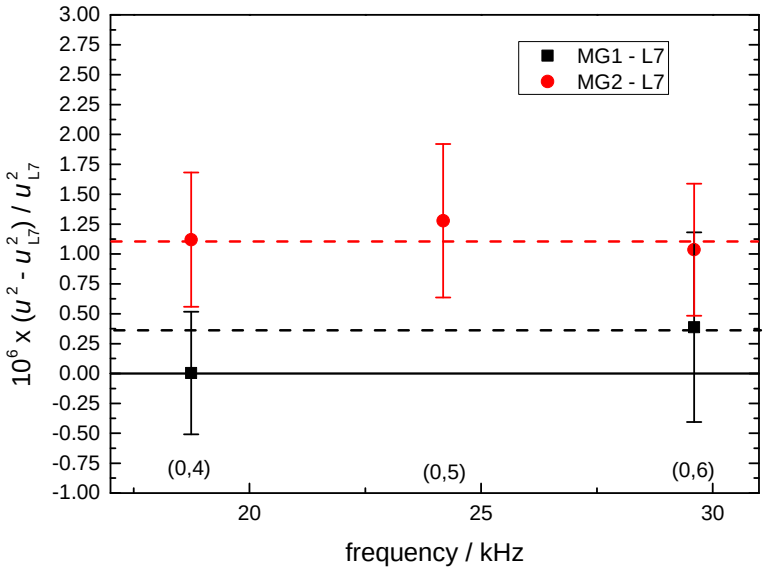

Figure 27. Relative differences between the squared speed of sound measured at 105 kPa, 273.16 K in two working helium samples (MG1 and MG2) and the reference value of the same quantity measured in sample L7, whose isotopic composition is known from the mass spectrometric analysis in Table 5.1. The observed differences are consistent with those expected (dashed lines) due to the different amounts of Ne and Ar impurities measured in the three samples (Table 5.1 and Table 5.2). The (0,5) mode datum for MG1 is not displayed on the plot because of its comparatively large uncertainty.

5.3 Estimate of outgassing

The results reported and discussed in the previous section refer to the estimated composition of our working sample of helium at a point of our gas manifold ("sampling point" in figure 9) which is located upstream of the resonator where the speed of sound is measured.

In this section we address the possible contamination of the sample due to outgassing from the metal surfaces to which the measurement volume is exposed, including the internal surface of the resonator itself. For AGT conducted at high temperature, the significant impact of hydrogen outgassing from stainless steel has been previously reported [54]. At ambient temperature and below, outgassing of water is a more likely cause of concern [25]. The influence of outgassing might be minimised by continuously flushing the internal measuring volume at a high flow rate. However, a systematic dependence of speed of sound on the flow-rate was previously reported for argon [3, 4], possibly due to thermal gradients induced by the expansion of the gas jet as it enters the cavity [15]. To assess such possible influence of the flow rate on the measured speed of sound, in a preliminary test at 300 kPa, 273.16 K, we varied the flow rate in four steps between 10 sccm and 100 sccm while continuously recording the resonance frequencies of three radial modes, observing no significant variation of the measurand within the limited relative precision of 0.3 ppm. This observation was confirmed, for flow rates up to 50 sccm, in another recent AGT experiment with helium [5].

Subsequently we conducted a test at the lower pressure of 105 kPa to enhance the effects of outgassing in no-flow conditions. We obtained a quantitative estimate of these effects by initially recording the frequency of mode (0,4) at a constant flow rate of 100 sccm, and subsequently stopping the flow and measuring the progressive negative drift of the frequency of mode (0,4) over 20

consecutive hours (figure 28). From a linear fit to the recorded relative variation we estimated $df_{(0,4)}/dt$ = 1.6 ppm/day. Assuming that this variation is caused by outgassing of water from the internal surface of the resonator, we calculated a corresponding outgassing rate of about 1.4×10^{-11} mol m^{-2} s^{-1}, which is compatible with typical outgassing rates of metal surfaces after extended evacuation [25]. We used this estimate to calculate the maximum possible concentration of water vapour x_{H_2O} in our working gas in our normal experimental conditions, i.e. while flowing at 100 sccm, with the result x_{H_2O} = 0.03 ppm and a corresponding possible effect on our estimate of M of −0.12 ppm. If our assumption that the observed drift of $f_{(0,4)}$ is caused by outgassing of water vapour is wrong, and the cause was instead a virtual leak of nitrogen from a small volume communicating with the resonator with a large impedance to flow, then the concentration of nitrogen in our working gas would be x_{N_2} = 0.02 ppm. We finally account for the possible effect of outgassing onto our estimate of M with a dedicated uncertainty contribution of 0.07 ppm (table 6).

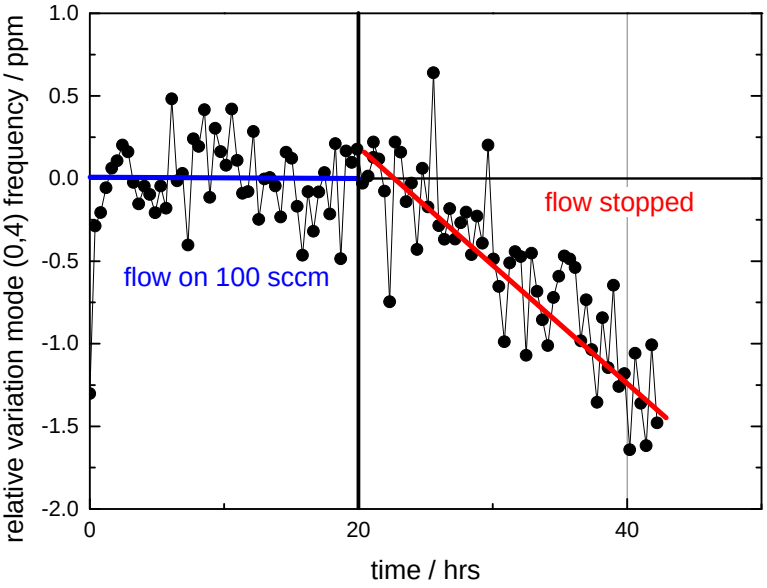

Figure 28. Relative variation of the resonance frequency of mode (0,4) at 105 kPa, 273.16 K over 40 hours of consecutive measurements. Flow rate is maintained constant at 100 sccm for the first 20 hours and then suddenly stopped. A water outgassing rate of about 1.4×10^{-11} mol m^{-2} s^{-1} is derived from the slope of the negative drift of the frequency as a function of time.

5.4 Determination of the molar mass of the working helium sample

The assumption $\mathfrak{X}_{MG2} = \mathfrak{X}_{L7}$ discussed in section 5.2, and the composition listed in table 5 for MG2 lead to our final estimate M_{MG2} = (4.002 6032 ± 0.000 0015) g mol^{-1}, where the reported uncertainty is the quadrature sum of the contributions listed in table 6. There, the relative contribution $u_r(M_{MG2})$ = 0.32 ppm of the uncertainty associated to the mass spectrometric analysis of impurities at PTB, was calculated using the sensitivity factors from table 2 in [15], the measurement uncertainty of a detected trace amount (13 ppb) of neon, and the detection limits for the possible undetected impurities Ar, Kr, Xe and H_2O. This calculation assumes an asymmetric rectangular distribution.

Table 6. Uncertainty budget of molar mass estimate

Source	$u(M)$ / g mol^{-1}	$u_r(M)$ / ppm	comments
Impurities in He	0.000 0013	0.32	section 5.1
Helium isotopic abundance	0.000 0007	0.17	section 5.2
Estimated outgassing	0.000 0003	0.07	section 5.3
Total (quadrature sum) M	**0.000 0015**	**0.37**	

6. Thermometry

To provide traceability to the current definition of the kelvin for our measurement of the temperature of the gas, we used three calibrated capsule-type standard platinum resistance thermometers (cSPRTs) in thermal contact with the shell of the resonator. In doing so, we assume that the thermal stability of our experiment was sufficient to relax any significant thermal gradient within the shell and that the relaxation time for the gas injected into the cavity to come into thermal equilibrium with the shell was sufficiently small. The slow temperature drifts which are typical of our apparatus, in the order of ± 1mK/day, compared to the time constant needed to record a complete set of acoustic and microwave data (25 mins) confirm the validity of the first assumption; the absence of changes in the measured frequencies and temperatures when the flow is abruptly switched from the normal operating conditions (100 sccm) to a no-flow condition (figure 28) support the second assumption.

With minor differences, the design features of the temperature control, the thermal enclosure surrounding the resonator within its containing vessel, the circulating liquid bath thermostat and the instrumentation and the procedures used for temperature measurements in this work are the same as previously described in section 4.1 of [55]. With respect to previously published AGT work at INRiM [20, 55], the relevant differences include the different material comprising the resonator, copper instead of stainless steel, and its larger dimensions and mass. In reason of the larger thermal conductivity of copper with respect to steel, this change was expected to reduce temperature gradients significantly, however this expectation was only partially confirmed in the course of the experiments.

6.1 Thermal gradients

The location of the three cSPRTs, respectively denoted HS156, HS157, and HS124 was approximately symmetrical along the vertical profile of the shell as illustrated in figure 3. The mean temperature of the resonator and the maximum difference in the temperature readings from the three thermometers was found to vary only slightly depending on the experimental pressure when the resonator and the vessel were filled with helium, but increased significantly when the resonator was evacuated (figure 29).

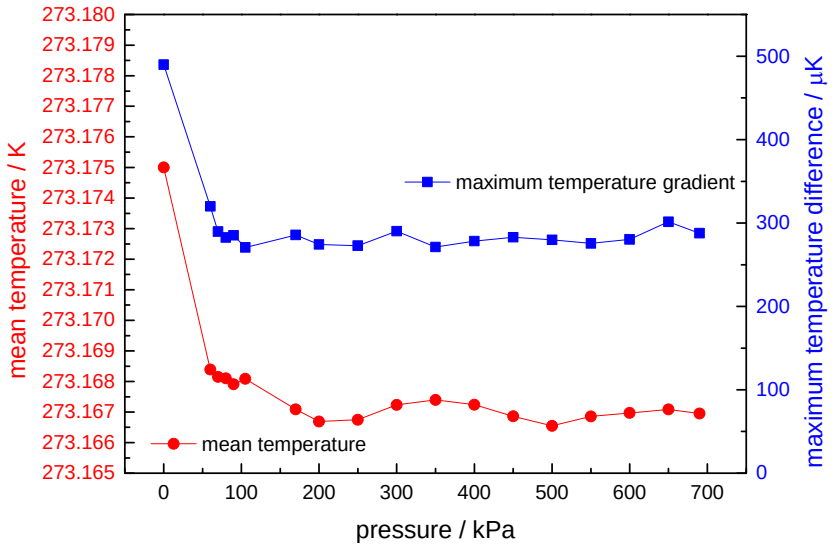

Figure 29. (left Y-axis, round symbols) Mean resonator temperature and maximum temperature difference measured across the resonator (right Y-axis, square symbols).

In both experimental conditions, HS124 (located in the bottom part of the shell) always indicated a higher temperature than HS157 (located slightly above the equatorial flange) and HS156 (located in the upper part of the shell); in vacuum, a vertical temperature gradient of ± 250 µK was found to be

symmetrical around the equator. When pressurized gas was admitted in the shell and the containing vessel, i.e. in the working experimental condition, the temperature difference between the lower and the upper part of the shell was 140 μK, while the temperature difference between the lower and the equatorial part of the shell was 290 μK. We interpreted all these observations as a possible indication of: i) vertical stratification of the temperature of the liquid bath surrounding the pressure vessel; ii) prevalence of a thermal link between the cavity and the bath by heat conduction through the gas contained within the vessel; iii) prevalence of a thermal link between the cavity and the bath by heat conduction through its mechanical support to the top lid of the vessel when the cavity and the vessel are evacuated. The reported thermal gradients were obtained by maximizing the depth of immersion of the pressure vessel within the bath and maximizing stirring of the liquid within the bath to remove stratification. We finally estimated the contribution of the thermal gradients (± 84 μK) to the uncertainty of our determination of the gas temperature by assuming a range of uniform probability for the readings of the cSPRTs, with $u_r(T) = 0.31$ ppm.

6.2 Calibration procedures and results

The three capsule cSPRTs were calibrated twice at the fixed points of the ITS-90 between the triple point of mercury and the freezing point of indium, as maintained at INRiM: in December 2013, before starting the AGT measurements reported in this work, and in December 2014 after their completion. In both occasions, calibration data were collected with the following measurement sequence: (1) triple point of water, T_{TPW}; (2) freezing point of indium T_{fIn} ; (3) T_{TPW}; (4) melting point of gallium, T_{mGa}; (5) T_{TPW}; (6) triple point of mercury T_{Hg}; (7) T_{TPW}. Calibration data at fixed points different from T_{TPW} were collected in view of using the AGT for T-T_{90} determinations over this temperature range. For calibration of the cSPRTs in the fixed point cells an adapter stem was used, allowing measurements with the usual instrumentation and procedures used for long-stem SPRTs. The temperature excursion up to the indium point was observed to cause some annealing effect on the resistance of the thermometers. Thus, only TPW readings after annealing were considered. After letting the TPW stabilize for about one week, after mantle creation, and checking for free rotation of the mantle, the resistance of each cSPRT was measured. Special care was taken for reaching adequate thermal equilibrium in the cell before taking data. The national standard for the triple point of water as maintained at INRiM is well characterized from international comparisons [56, 57] with an estimated uncertainty of 20 μK. The resistance values for each thermometer were corrected to account for the immersion depth in the cell, self heating and isotopic composition (table 7). During resistance measurements the short term stability amounted to 10 μK corresponding to 0.04 ppm.

From the comparison of repeated calibrations at the TPW for each cSPRT, we determine two additional uncertainty contributions to our estimate of T: i) a contribution, denoted *repeatability within calibration sequence*, which represents the repeatability of the results at T_{TPW} in the course of each calibration sequence, where the estimate 0.07 mK is the mean for the three cSPRTs; ii) a contribution, denoted *thermometer stability*, from the comparison of the 2013 and 2014 calibration results. For the three SPRTs a relative variation was found of 0.094 mK for HS157, 0.164 mK for HS156, −0.046 mK for HS 124. We used these data to calculate a correction to T_{Exp} corresponding to half the mean variation for the three cSPRTs, i.e. (0.036 ± 0.030) mK, equivalent to (0.13 ± 0.11 ppm (table 7).

6.3 Resistance measurements

Three different resistance bridges, $F900_{cal}$, $F18_{cal}$ and $F18_{Exp}$, were involved for the temperature calibrations and measurements related to this work. $F900_{cal}$ was used for the initial calibrations in 2013, but it was no longer available and it was substituted by $F18_{cal}$ when the ex-post calibration was

carried out in 2014. $F18_{Exp}$ was used for temperature readings associated with the acoustic and microwave measurements discussed in this work. To minimize the measurement uncertainty we adopted the same bridge settings (carrier frequency 25 Hz, sensor current 2 mA, 100 Ω impedance, 10^4 gain, 10 Hz bandwidth) during both calibrations and measurement. Also, the same 100 Ω Standard Resistor (R100) was employed for both calibrations and measurements (a 100 Ω Standard Resistor was needed for scheduled calibration and measurements up to the Indium point, where the cSPRTs resistance is about 41 Ω).

As a major drawback of this choice of instrumentation and procedures, we discovered that the three bridges read significantly different values of the ratio R25/R100 between the same 25 Ω standard resistor (R25) and the aforementioned 100 Ω resistor. These systematic differences in reading our reference ratio R25/R100 were found to be extremely repeatable by the following relative amounts: $(F900_{cal} - F18_{cal}) = (0.48 \pm 0.03)$ ppm and $(F900_{cal} - F18_{Exp}) = (-0.31 \pm 0.09)$ ppm. We used the estimated difference $(F900_{cal} - F18_{cal})$ to correct calibration results in 2013 and 2014 before their comparison as discussed in the previous section. We used the estimated difference $(F900_{cal} - F18_{Exp})$ to calculate an additional correction to T_{Exp}, with an additional relative uncertainty contribution of 0.09 ppm.

6.4 Thermometry uncertainty budget

Table 7. Uncertainty budget of relevant uncertainty contributions deriving from thermometry

Quantity	Estimate or rel. correction	$u(T)$ / mK	$u_r(T)$ / ppm	Comments
Thermal gradients		0.084	0.31	section 6.1
T_{TPW}	273.1600 K	0.020	0.07	international comparisons
Immersion	0.17 mK	0.007	0.03	
Repeatability within calibration sequence		0.070	0.26	
Self heating - calibration	2.5 mK	0.006	0.02	section 6.2
Short-term repeatability		0.010	0.04	
Self heating - measurement	2.4 mK	0.006	0.02	
Long term stability (correction)	-0.13×10^{-6}	0.030	0.11	section 6.2
Systematics R25/R100 bridges (correction)	0.31×10^{-6}	0.025	0.09	section 6.3
Total (quadrature sum) T_{Exp}	273.160 05 K	**0.115**	**0.42**	

7. Concluding remarks

The present determinations of R and k are consistent with most other recent accurate results obtained by AGT or other experimental techniques and the 2010 CODATA recommended values (figure 1). However, they are slightly inconsistent with our previously published results, which were based on speed of sound measurements in helium at a single thermodynamic state [20]. In retrospect, we suspect that those previous results may have been biased by an underestimate of the molar mass of the helium sample and/or by the imperfect acoustic model. The contribution of these two sources of uncertainty were substantially reduced in this work, increasing confidence that the results presented in this work should supersede those previously published.

Speculating about possible future improvements of the AGT technique, we observe that the imperfect acoustic performance of our experiment still represents the most relevant contribution to the overall uncertainty budget. Some practical design modifications, including the use of alternative geometries for the realization of resonators (cylinders or spherical shells with increased wall thickness) and the use of low admittance acoustic waveguides in place of condenser microphones, were recently suggested in [15]. The future adoption of these design features may reduce the uncertainty contributions of acoustics, while reducing the economic cost and the modelling and experimental effort at levels which would be more acceptable for practical applications of AGT. Also, we believe that the advantages of using helium as the working gas of an AGT - thermophysical and electrical properties calculable from theory, minor variability of the isotopic composition - may overcome the disadvantages – extreme sensitivity to common impurities. With foresight, we believe that a sealed resonant cavity containing helium maintained in permanent contact with a suitable getter material would be useful for practical AGT.

Acknowledgements

This work would not have been possible without the significant cooperation, information and support received by Laurent Pitre and Michael de Podesta and their co-workers at LNE/Cnam and NPL. The authors are grateful to Michael Moldover for first suggesting strategies which improved the final performance of the experimental technique, and for continuous encouragement. Also, this work benefitted from frequent discussions with Jim Mehl and Keith Gillis, who additionally shared their work and results as soon as they became available. At NPL, we thank David Flack for his careful CMM characterization of our cavity. At PTB, the assistance of Thorsten Zandt for mass spectrometric analysis was fundamental. We are indebted with many colleagues at INRiM for equipment loan and sharing of expertise and facilities; particularly, we wish to thank Alberto Giuliano Albo for the regression of CMM data, Stefano Pasqualin, Fabio Bertiglia, Mercede Bergoglio for the particular care which they dedicated to the calibration of our instrumentation, Elisabetta Chirivì for assistance with the measurements, and Marco Bertinetti for prompt, constant help and assistance at the mechanical workshop of INRiM. Finally, we are grateful to Gregoire Bastin who was responsible at Savimex for the mechanical realization of our resonator with care and commitment going far beyond commercial obligations.

At different stages of its development this work was funded by the iMERA+ and EMRP joint research programmes of the European Union. This work was completed within the unfunded cooperative framework of activities fostered by the EURAMET Project 885.

References

[1] Mills I M, Mohr P J, Quinn T J, Taylor B N and Williams E R 2006 Redefinition of the kilogram, ampere, kelvin and mole: a proposed approach to implementing CIPM recommendation 1 (CI-2005) *Metrologia* **43** 227-46

[2] de Podesta M, Underwood R, Sutton G, Morantz P, Harris P, Mark D F, Stuart F M, Vargha G and Machin G 2013 A low-uncertainty measurement of the Boltzmann constant *Metrologia* **50** 354–76

[3] de Podesta M, Yang I, Mark D F, Underwood R, Sutton G and Machin G 2015 Correction of NPL-2013 estimate of the Boltzmann constant for argon isotopic composition and thermal conductivity (submitted to *Metrologia*)

[4] Pitre L, Sparasci F, Truong D, Guillou A, Risegari L and Himbert M E 2011 Measurement of the Boltzmann constant k_B using a quasi-spherical acoustic resonator *Int. J. Thermophys.* **32** 1825–86

[5] Pitre L, Sparasci F, Truong D, Guillou A, Risegari L, Himbert M E and Giuliano Albo P A 2014 Determination of the Boltzmann constant *k* from speed of sound in helium gas at the triple point of water (submitted to *Metrologia*)

[6] Moldover M R, Trusler J P M, Edwards T J, Mehl J B and Davis R S 1988 Measurement of the universal gas constant *R* using a spherical acoustic resonator *J. Res. Natl Bur. Stand.* **93** 85–144

[7] Gaiser C, Zandt T, Fellmuth B, Fischer J, Jusko O and Sabuga W 2013 Improved determination of the Boltzmann constant by dielectric-constant gas thermometry *Metrologia* **50**: L7-L11

[8] Schmidt J W, Gavioso R M, May E F and Moldover M R 2007 Polarizability of Helium and Gas Metrology *Phys. Rev. Lett.* **98** 254504

[9] Qu J, Benz S P, Pollarolo A, Rogalla H, Tew W L, White R and Zhou K 2015 Improved electronic measurement of the Boltzmann constant by Johnson noise Thermometry (submitted to *Metrologia*)

[10] Castrillo A, Moretti L, Fasci E, De Vizia M D, Casa G and Gianfrani L 2014 The Boltzmann constant from the shape of a molecular spectral line *J. Mol. Spectros.* **300** 131-38

[11] Rohart F, Mejri S, Sow P L T, Tokunaga S K, Chardonnet C, Darquié B, Dinesan H, Fasci E, Castrillo A, Gianfrani L and Daussy C 2014 Absorption-line-shape recovery beyond the detection-bandwidth limit: Application to the precision spectroscopic measurement of the Boltzmann constant *Phys. Rev. A* **90**, 042506

[12] Ripple D C, Davis R, Fellmuth B, Fischer J, Machin G, Quinn T, Steur P, Tamura O and White D R 2010 The Roles of the *Mise en Pratique* for the Definition of the Kelvin *Int. J. Thermophys.* **31** 1795-1808

[13] Moldover M R, Gavioso R M, Mehl J B, Pitre L, de Podesta M and Zhang J T 2014 Acoustic gas thermometry *Metrologia* **51** R1-R19

[14] Mohr P J, Taylor B N and Newell D B 2012 CODATA recommended values of the fundamental physical constants *Rev. Mod. Phys.* **84** 1527-1605

[15] Mohr P J, Taylor B N and Newell D B 2008 CODATA recommended values of the fundamental physical constants *Rev. Mod. Phys.* **80** 633-730

[16] Pitre L, Guianvarc'h C, Sparasci F, Guillou A, Truong D, Hermier Y and Himbert M E 2009 An improved acoustic method for the determination of the Boltzmann constant at LNE-INM/CNAM *C. R. Pysique* **10** 835-48.

[17] Sutton G, Underwood R, Pitre L, de Podesta M and Valkiers S 2010 Acoustic resonators experiments at the triple point of water: first results for the Boltzmann constant and remaining challenges *Int. J. Thermophys.* **31** 1310–46

[18] Gavioso R M, Benedetto G, Albo P A G, Ripa D M, Merlone A, Guianvarc'h C, Moro F and Cuccaro R 2010 A determination of the Boltzmann constant from speed of sound measurements in helium at a single thermodynamic state *Metrologia* **47** 387–409

[19] Zhang J T, Lin H, Feng X J, Sun J P, Gillis K A, Moldover M R and Duan Y Y 2011 Progress toward re-determining the Boltzmann constant with a fixed-path-length, cylindrical resonator *Int. J. Thermophys.* **32** 1297–329

[20] Lin H, Feng X J, Gillis K A, Moldover M R, Zhang J T, Sun J P and Duan Y Y 2013 Improved determination of the Boltzmann constant using a single, fixed-length cylindrical cavity *Metrologia* **50** 417–32
[21] Underwood R, Flack D, Morantz P, Sutton G, Shore P and de Podesta M 2011 Dimensional characterization of a quasispherical resonator by microwave and coordinate measurement techniques *Metrologia* **48** 1–15
[22] de Podesta M, May E F, Mehl J B, Pitre L, Gavioso R M, Benedetto G, Giuliano Albo P A, Truong D and Flack D 2010 Characterization of the volume and shape of quasi-spherical resonators using coordinate measurement machines *Metrologia* **47** 588–604
[23] Underwood R, Mehl J B, Pitre L, Edwards G, Sutton G and de Podesta M 2010 Waveguide effects on quasispherical microwave cavity resonators *Meas. Sci. Technol.* **21** 075103
[24] Moldover M R, Boyes S J, Meyer C W, Goodwin A R H 1999 Thermodynamic temperatures of the triple points of mercury and gallium and in the interval 217 K to 303 K *J. Res. Natl Inst. Stand. Technol.* **104** 11–46
[25] de Podesta M, Sutton G, Underwood R, Bell S, Stevens M, Byrne T and Josephs-Franks P 2011 Outgassing of water vapour, and its significance in experiments to determine the Boltzmann constant *Metrologia* **48** L1–L6
[26] Mehl J B 2009 Second-order electromagnetic eigenfrequencies of a triaxial ellipsoid *Metrologia* **46** 554–9
[27] Mehl J B 2015 (submitted) Second-order electromagnetic eigenfrequencies of a triaxial ellipsoid II.
[28] Edwards G, Underwood R J 2011 The electromagnetic fields of a triaxial ellipsoid calculated by modal superposition *Metrologia* **48** 114–22
[29] Hurly J J, Moldover M R 2000 Ab Initio Values of the Thermophysical Properties of Helium as Standards *J. Res. Natl. Inst. Stand. Technol.* **105**, 667–88
[30] Cencek W, Komasa J and Szalewicz K 2011 Collision-induced dipole polarizability of helium dimer from explicitly correlated calculations *J. Chem. Phys.* **135** 014301
[31] Cencek W, Przybytek M, Komasa J, Mehl J B, Jeziorski B and Szalewicz K 2012 Effects of adiabatic, relativistic, and quantum electrodynamics interactions on the pair potential and thermophysical properties of helium *J. Chem. Phys.* **136** 224303
[32] Garberoglio G, Moldover M R and Harvey A H 2011 Improved first principles calculation of the third virial coefficient of helium *J. Res. Nat. Inst. Stand. Technol.* **116** 729–42
[33] Łach G, Jeziorski B and Szalewicz K 2004 Radiative corrections to the polarizability of helium *Phys. Rev. Lett.* **92** 233001
[34] Bruch L W and Weinhold F 2000 Diamagnetism of helium *J. Chem Phys.* **113** 8667–70
[35] Rizzo A, Hättig C, Fernandez B and Koch H 2002 The effect of intermolecular interactions on the electric properties of helium and argon: III. Quantum statistical calculations of the dielectric second virial coefficients *J. Chem. Phys.* **117** 2609–18
[36] D. F. Heller and W. M. Gelbart, 1974 Short range electronic distortion and the density dependent dielectric function of simple gases *Chem. Phys. Lett.* **27**, 359–64
[37] Schmidt J W and Moldover M R 2003 Dielectric permittivity of eight gases measured with cross capacitors *Int. J. Thermophys.* **24** 375–403
[38] May E F, Pitre L, Mehl J B, Moldover M R and Schmidt J W 2004 Quasi-spherical resonators for metrology based on the relative dielectric permittivity of gases *Rev. Sci. Instrum.* **75** 3307–17
[39] Gillis K A, Shinder I I and Moldover M R 2004 Thermoacoustic boundary layers near the liquid–vapor critical point *Phys. Rev.* E **70** 021201
[40] Wieser M E and Berglund M 2009 Atomic weights of the elements 2007 (IUPAC Technical Report) *Pure Appl. Chem.* **81** 2131–56
[41] Gillis K A 2012 Second-order boundary corrections to the radial acoustic eigenvalues for a spherical cavity *Metrologia* **49** L21–4
[42] Gavioso R M, Benedetto G, Madonna Ripa D, Giuliano Albo P A, Guianvarc'h C, Merlone A, Pitre L, Truong D, Moro F and Cuccaro R 2011 Progress in INRiM experiment for the determination of the Boltzmann constant with a quasi-spherical resonator *Int. J. Thermophys.* **32** 1339–54

[43] Moldover M R, Mehl J B and Greenspan M 1986 Gas-filled spherical resonators—theory and experiment *J. Acoust. Soc. Am.* **79** 253–72
[44] Hands B A and Arp V D 1981 A correlation of thermal conductivity data for helium *J. Phys. Chem. Ref. Data* **28** 779–850, as implemented in the computer package: Lemmon E W, McLinden M O and Huber M L 2010 *REFPROP: Reference Fluid Thermodynamic and Transport Properties* NIST Standard Reference Database 23, Version 8.0 (Boulder, CO: National Institute of Standards and Technology) www.nist.gov/srd/nist23.cfm
[45] Kestin J, Paul R, Clifford A A and Wakeham W A 1980 Absolute determination of the thermal conductivity of the noble gases at room temperature up to 35 MPa *Physica* A **100** 349–69.
[46] Ewing M B, McGlashan M L and Trusler J P M 1986 The temperature-jump effect and the theory of the thermal boundary layer for a spherical resonator. Speeds of sound in argon at 273.16K *Metrologia* **22** 93–102
[47] Waelbroeck F G and Zuckerbrodt P 1958 Thermal Conductivities of Gases at Low Pressures. I. Monatomic Gases, Helium and Argon *J. Chem. Phys.* **28**, 523-24
[48] Semionov Y G, Borisov S F, Suetin P E 1984 Investigation of heat transfer in rarefied gases over a wide range of Knudsen numbers *Int. J. Heat Mass Transfer*, **27** 1789-1799
[49] Mehl J B 1985 Spherical acoustic resonator: effects of shell motion *J. Acoust. Soc. Am.* **78** 782–8
[50] Mehl J B 2007 Acoustic Eigenvalues of a Quasispherical Resonator: Second Order Shape Perturbation Theory for Arbitrary Modes *J. Res. Natl Inst. Stand. Technol.* **112** 163–73
[51] Gillis K A, Lin H and Moldover M R 2009 Perturbations from ducts on the modes of acoustic thermometers *J. Res. Nat. Inst. Stand. Technol.* **114** 263–85
[52] Rodrigues D, Guianvarc'h C, Durocher J N, Bruneau M and Bruneau A M 2008 A method to measure and interpret input impedance of small acoustic components *J. Sound Vib.* **315** 890–910
[53] Guianvarc'h C, Gavioso R M, Benedetto G, Pitre L and Bruneau M 2009 Characterization of condenser microphones under different environmental conditions for accurate speed of sound measurements with acoustic resonators *Rev. Sci. Instrum.* **80** 074901
[54] Ripple D C, Defibaugh D R, Moldover M R and Strouse G F 2003 Techniques for primary acoustic thermometry to 800K *TEMPERATURE: Its Measurement and Control in Science and Industry* vol VII; *8th Int. Temperature Symp. (Chicago IL, 21–24 October 2002)* ed D C Ripple (New York: AIP) pp 25–30
[55] Benedetto G, Gavioso R M, Spagnolo R, Marcarino P and Merlone A 2004 Acoustic measurements of the thermodynamic temperature between the triple point of mercury and 380K *Metrologia* **41** 74–98
[56] Stock M, Solve S, del Campo M D, Chimenti V, Méndez-Lango E, Liedberg H, Steur P P M, Marcarino P, Dematteis R, Filipe E, Lobo I, Kang K H, Gam K S, Kim Y G, Renaot E, Bonnier G, Valin M, White R, Dransfield T D, Duan Y, Xiaoke Y, Strouse G, Ballico M, Sukkar D, Arai M, Mans A, de Groot M, Kerkhof O, Rusby R, Gray J, Head D, Hill K, Tegeler E, Noatsch U, Duris S, Kho H Y, Ugur S, Pokhodun A, and Gerasimov S F 2006 Final Report on CCT-K7: Key comparison of water triple point cells *Metrologia* Tech. Suppl. **43** 03001.
[57] Peruzzi A, Bosma R, Kerkhof O, Peter R, del Campo Maldonado M D, Smid M, Zvizdic D, Nielsen M B, Anagnostou M, Grudnewicz E, Nedea M, Steur P P M, Filipe E, Lobo I, Antonsen I, Renaot E, Weckstrom T, Bojkovski J, Turzó-András E, White M, Tegeler E, Dobre M, Ranostaj J, Kartal Dogan A, Augevicius V, Pokhodun A and S Simic 2006 Final Report on EUROMET.T-K7: Key comparison of water triple point cells *Metrologia* Tech. Suppl. **46** 03001.